Pulsed laser deposition of complex transition metal oxides: plume expansion and film growth

Alessia Sambri

Contents

Introduction

The complex transition metal oxides have attracted a huge interest in the last 20 years, since such compounds can exhibit a large variety of interesting properties, simply by structural and compositional tuning. The versatility of these compounds for electronic applications is demonstrated by the fact that, in this set, one can find materials whose conduction properties are anywhere in between highly conducting metallic, and in some cases superconducting, to high-k dielectric and insulating. One can find non-magnetic materials as well as magnetic compounds with almost any kind of magnetic order. Moreover, it can be found ferro- and ferri- magnets as well as antiferromagnets. A wide range of electronic device applications is foreseen for perovskite oxide families, as summarized in Figure 1.

However there are still some questions to be answered and some material problems to be solved in order to employ the physical properties of these compounds in competitive electronics. Namely, in transition metal oxides the nature of the physical properties is often associated to very short length scales and the magnetic and electronic properties are strongly influenced by charge carrier density. The charge carrier density can be varied through chemical doping giving rise to a very complex phase diagram, as function

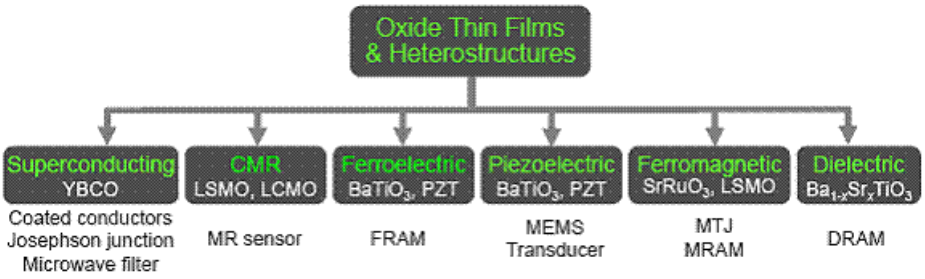

Figure 1: Novel electronic device applications based on the different physical properties of perovskite-structured oxides.

of the dopant concentration. Unfortunately the chemical doping introduces disorder and structural modification in epitaxial thin films that, in turn, affect the physical properties.

The considerations reported above show that, once chosen the bulk material for its intrinsic physical properties, the performances of the fabricated devices are strongly determined by structural properties (domain structures, roughness, microstructure) and chemical composition, such as the oxygen content [1].

This means that to reach the goal of a possible application of such intriguing materials in electronics, a very careful control in the device fabrication process is required. In particular, since the integration in the electronic and spintronic devices is frequently by means of thin film multilayered heterostructures, an extreme control of the film growth process is needed, in order to obtain high quality interfaces. Moreover, in the case of heteroepitaxial growth, there always exist an unavoidable compressive or tensile strain in the films, due to the lattice mismatch between film and substrate and/or the thermal expansion misfit between the film and the substrate compounds. Since the strain effect induces a deformation of the unit cell, modifying the film physical properties with respect to the bulk compound, an atomic scale control of the film growth kinetics it is necessary for possible future application of complex oxides compounds in the electronic and spintronic devices and in sensor technologies.

Despite the rapid progress of high-quality crystal growth techniques has enabled the fabrication of superlattices of perovskite oxides, some aspects of the film growth process are still unclear and the approach to the deposition of each new material or to the realization of complex multilayered structures is empiric.

Among the deposition techniques, the pulsed laser deposition (PLD) it is one of the widely used technique in oxides thin film deposition. Its offers a relative simplicity in controlling the deposition rate and in obtaining the correct stoichiometric transfer of the material form the *bulk* to the deposited film. The deposition of oxides takes place in a well controlled oxygen atmosphere, allowing oxygen incorporation in the growing film. In fact, it is well known that the oxygen deficiency in oxide thin films affects the electronic device performances such as leakage current in capacitors and leaky barrier in tunnel junctions.

In spite of the considerable effort made to control and optimize the pulsed laser deposition process of complex oxides, it is still unclear how deposition parameters such as ambient pressure, target substrate distance, substrate temperature, type of substrate etc. can induce the morphological disorder, as surface roughening. This is because there are not many simple model

systems in oxides, compared to other materials.

In particular, an open question still widely discussed [2], [3], [4], [5] concerns how the ablated species dynamics affects the thin film growth. In fact, even if it is rather established that the energy of the flux of hyperthermal particles impinging on the growth surface provides an extra contribution to the adatom mobility, beside the thermal energy supplied to the system by substrate heating, a deep understanding of the influence of the plume physical properties on film growth is still missing.

This thesis represents a first attempt aiming to a quantitative understanding of the correlations between plasma plume parameters and thin film properties. In particular, the study was focused on the plasma plume propagation through the background atmosphere in different conditions of deposition (namely oxygen pressure and substrate temperature), while looking for the corresponding variation induced on the film growth, monitored by High-pressure Reflection High Energy Electron Diffraction (RHEED) technique.

The research activity of the thesis was developed on a new modular facility for oxides deposition and analysis (MODA Modular facility for Oxides Deposition and Analysis), on which all the following work was done. The facility consists in a multichamber UHV system, devoted to the growth of different materials by PLD and the characterization the surface properties of as-grown uncontaminated samples by means of STM (Scanning Tunnel Microscopy) and AFM (Atomic Force Microscopy), LEED (Low Energy Electron Diffraction) and XPS (X-ray Photoemission Spectroscopy) techniques.

Among the very wide class of complex transition metal oxides, this work focus on $La_{0.7}Sr_{0.3}MnO_3$ and $SrTiO_3$ compounds. With a view on potential technological applications, the $La_{0.7}Sr_{0.3}MnO_3$ compound shows two intriguing properties: the so called *colossal magneto resistance* (CMR) and a *half-metallic* behavior. Namely, the first effect consists in a huge change in the electrical resistivity induced by an external magnetic field, while the second involves a fully spin-polarized conduction current. These two features can potentially be used to make magnetic storage devices, single-spin electron sources, spin valves, non-volatile magnetic random access memories (MRAM) based on a magnetic tunnel junction (MTJ)[6],[7] and high-efficiency magnetic sensors.

Also the $SrTiO_3$ compound exhibits several unexpected and intriguing properties, as quantum paraelectricity, record-high permittivity (up to 10^4 at 10K) [36], ferroelectricity induced by compressive biaxial strain [37] or by isotopic substitution [38], making such oxide a promising candidate in technological applications. Furthermore, the $SrTiO_3$ compound is widely employed as substrate in deposition of oxides thin film, for its chemical and compositional stability and for its lattice constant, well matched to the lat-

tices parameters of a wide class of perovskites oxides compounds.

The thesis is divided into six Chapters, describing the details of my scientific research and the experimental results. The first phase of my PhD activity, including the participation to set-up MODA facility and the optimization of the deposition parameters for high quality $La_{0.7}Sr_{0.3}MnO_3$ and $SrTiO_3$ films is not described here.

In Chapter 1 a brief overview on the crystal structure and the physical properties of $La_{0.7}Sr_{0.3}MnO_3$ and $SrTiO_3$ is given.

In Chapter 2 the details of MODA instrumental endowment and the descriptions of the various available surface analysis techniques are reported.

In Chapter 3 the pulsed laser ablation phenomenon is discussed in details, from the laser–target interaction, through the plasma formation and expansion, up to the film nucleation and growth.

In Chapter 4 the $La_{0.7}Sr_{0.3}MnO_3$ and $SrTiO_3$ plasma plume expansion results are presented. I performed measurements of the expanding plasma plume by time gated photography during the pulsed laser deposition, in different experimental conditions (O_2 pressure value and substrate temperature). This was performed by resorting to a fast ICCD (Intensified Charge Couple Device) camera, recording the optical emission of the ablated species from the ablation event up to the deposition of the species on the substrate. From a software analysis of the acquired 2D images of the plume, I extrapolated plume dynamics parameters, such as the stopping distance and the impact kinetic energy, with respect to the oxygen pressure or the substrate temperature. In fact, beside evidencing the braking effect on plume expansion due the deposition gas, our data revealed also an indirect effect on the plume dynamic due to the deposition temperature that is discussed and interpreted by a simple plume expansion model.

In Chapter 5 the results of RHEED measurements on film growth, as a function of the deposition pressure are presented. The aim of such measurements was to evaluate the effect on the film growth mode of different kinetic contributions of the ablated species impinging on the target, since our results on plume expansion dynamics clearly show that the background oxygen affects their average kinetic energy. The RHEED measurements were performed recording the intensity variation of (0,0), (0,1) and (0,-1) spots, during the $SrTiO_3$ film deposition, for different values of oxygen pressure. Despite the high quality obtained in $La_{0.7}Sr_{0.3}MnO_3$ films, no RHEED measurement on such material is here presented because, in case of heteroepitaxy, not only the kinetic factors, but also thermodynamic factors, as misfit or differences in thermal coefficients, are relevant in determining the growth mode.

The results obtained by monitoring the film growth for each value of deposition pressure investigated, were interpreted by means of the results on

plume expansion dynamics achieved by time gated fast photography technique. The cross-correlation between the experimental results, obtained using complementary techniques focusing on the two distinct fundamental stages of the laser deposition process, such as the plume expansion and the film growth, are discussed in the conclusion section.

Chapter 1

Materials: $La_{0.7}Sr_{0.3}MnO_3$ and $SrTiO_3$

1.1 Perovskite structure materials

Both the studied $La_{0.7}Sr_{0.3}MnO_3$ and $SrTiO_3$ compounds belong to the perovskite oxides family, with general formula is ABO_3, where A is an alkaline earth ion and B is a transition metal cation.
In first approximation, the crystal structure can be viewed as a FCC (Faces Centered Cube) lattice with B-site cation at the center surrounded by six O-site anions, forming an octahedric structure, and four A-site cations, each at the corner, as shown in Figure 1.1.

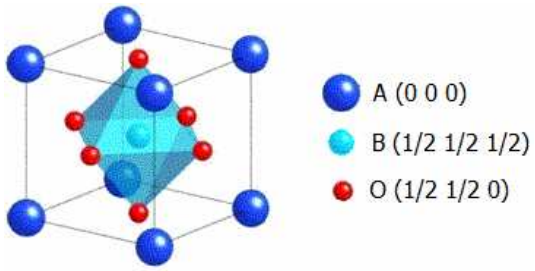

Figure 1.1: Crystal structure of a cubic perovskite: inside the cube with A-type atoms on the corners, it is placed the octahedron oxygen box, in which the B-type atom is embedded.

As matter of fact, for the majority of perovskite compounds the unit cell is a distorted FCC structure, corresponding to a distorted BO_6 octahedron. Distorted perovskite oxides can be stable, according to two criteria: charge

neutrality and structural stability. Charge neutrality is determined by the selection of ions with proper valence states, while structural stability is defined by a tolerance factor, expressed as:

$$TF = \frac{(R_A + R_O)}{\sqrt{2}\,(R_B + R_O)} \tag{1.1}$$

where R_A and R_B are the ionic radii of cations A and B, respectively. A tolerance factor TF = 1 corresponds to a perfect cubic structure, while 1.1>TF>0.8 represents a pseudocubic structure (that is tetragonal, orthorombic etc.). Stable perovskite structure is found for TF values in the range from 0.8 to about 1.1 [8], [9].
The unit cell distortion corresponds to the change in the angle of B–O–B, from 180°, in the case of TF=1, to 140°, in the case of TF=0.8.

By doping the perovskites compound, varying the cations on A and/or B sites is possible to induce a deformation on the unit cell structure, which effect is strongly related to the size of the substituted atoms in A and/or B site. The corresponding distortion in the octahedral BO_6 structure gives rise, in turn, to the occurrence of different electronic properties [10].

1.2 $La_{0.7}Sr_{0.3}MnO_3$

In $La_{0.7}Sr_{0.3}MnO_3$ the tolerance factor is TF = 0.983, corresponding to a rombohedric structure. However the deviation from cubic symmetry is rather small (see Figure 1.2), and in a first approximation the ideal cubic perovskite structure can be assumed. Therefore in many cases, especially when discussing thin films, a pseudo-cubic notation is used to describe the lattice parameter of the (bulk) manganite.

The transition metal, mixed valency Mn ion 3+ or 4+ (having 3d - outer orbitals) is coordinated with six oxygen ions. The hybridization and the electrostatic interaction with oxygen p electrons give rise to a crystal field and quenches the orbital angular momentum. These effects field lift the 5-fold degeneracy of d electrons present in free Mn^{3+} ions by splitting the 3d-orbital and forming a lower lying triply degenerate t_{2g} states and a higher doublet of e_g states, as shown in Figure 1.3.

The t_{2g} triplet consists of the d_{xy}, d_{xz} and d_{yz}-orbitals, while the e_g doublet contains the $d_{x^2-y^2}$ and $d_{3z^2-r^2}$ orbitals.

The filling of these levels follows Hund's first rule where parallel spins are energetically favorable due to minimization of Coulomb repulsion energy. In

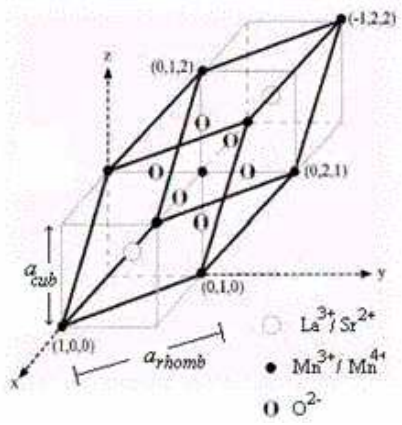

Figure 1.2: $La_{0.7}Sr_{0.3}MnO_3$ unit cell.

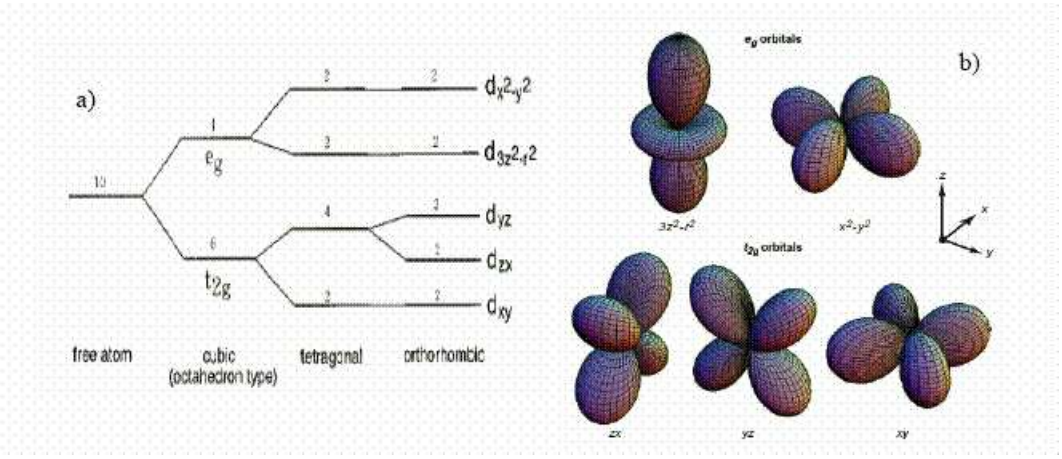

Figure 1.3: (a) Crystal field lifts the degeneracy of the d5 -electrons of the Mn^{3+} - ions into a t_{2g} triplet and an e_g doublet, further lifted by the Jahn Teller effect, discussed in the following. (b) The d_{xy}, d_{xz} and d_{yz}-orbitals correspond to the t_{2g} triplet, while to the e_g doublet the $d_{x^2-y^2}$ and $d_{3z^2-r^2}$ orbitals correspond.

practice, a strong Hund coupling between the t_{2g} and the e_g states leads to the formation of a high-spin state for the four 3d-electrons in the Mn^{3+} ion. The degeneracy of the t_{2g} and e_g is further lifted by the lattice deformations that lower the crystal symmetry. This effect, known as Jahn Teller effect [11], is due to the distortion of the MnO_6 octahedron structure that implys a further split of the e_g and t_{2g} degenerate orbital levels. In practice, a lowering of the energy of the $d_{3z^2-r^2}$ orbital is created with the compression of the O6-

octahedron in one direction while the perpendicular plane is expanded.

As consequence, considering the generic $La_{1-x}Sr_xMnO_3$ compound the following schematization can be taken into account: in the case of doping x=0, the valence of Mn is 3+ and the electron in the doublet e_g will occupy the $d_{3z^2-r^2}$ orbital, corresponding to a lower energy. When the doping is x=1, the ion Mn assumes valence 4+, the doublet e_g is empty and the MnO_6 octahedron is not distorted. As to say, while the Mn^{3+} ion is Jahn-Teller active, Mn^{4+} is not, hence the holes introduced by doping will ideally maintain the oxygen octahedron in a cubic symmetry [12],[9]. In the case of $La_{0.7}Sr_{0.3}MnO_3$ compound, where the Mn exhibits the double valence Mn^{3+}/Mn^{4+}, the perovskite cell is dynamically distorted by the electron *hopping*, creating a system characterized by a strong phonon–electron coupling [9], [12], [13].

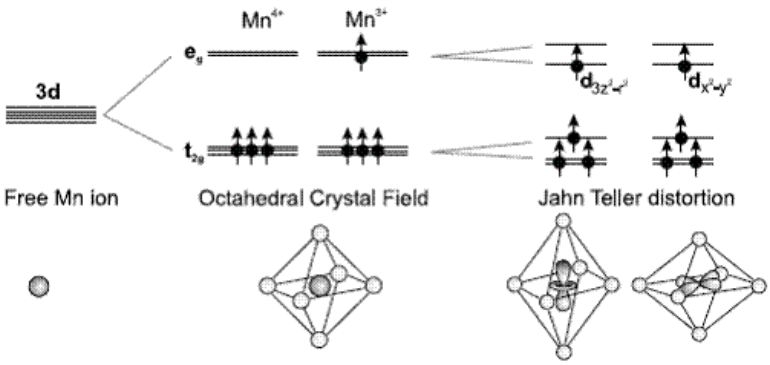

Figure 1.4: Jahn Teller Effect

In the frame of the Double Exchange (DE) mechanism [14], the carriers may hop through the bridging oxygen ion of the Mn^{3+} – O – Mn^{4+} bond. For the Hound 's rule, the 3d electrons have the same spin orientation, that is the three t_{2g} electrons in the case of Mn^{4+} and the three t_{2g} electrons plus the e_g electrons in the case of Mn^{3+}.

The e_g electron hopping from two contiguous ion Mn^{3+}/ Mn^{4+} can take place only if the spin orientation of the core electrons is the same, with a probability given by:

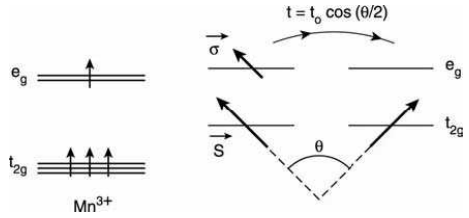

Figure 1.5: Schematic view of the DE mechanism

$$t = t_0 \cos\left(\frac{\theta}{2}\right) \tag{1.2}$$

where θ is the angle between the t_{2g} spins of neighbouring Mn^{3+}/ Mn^{4+} ion [12], [9] (see Figure 1.5). The evidence that the probability has a maximum for θ=0 and a minimum for θ=π reveals the ferromagnetic behavior of the double-exchange interaction.

In Figure 1.6 the phase diagram for the generic $La_{1-x}Sr_xMnO_3$ compound is depicted.

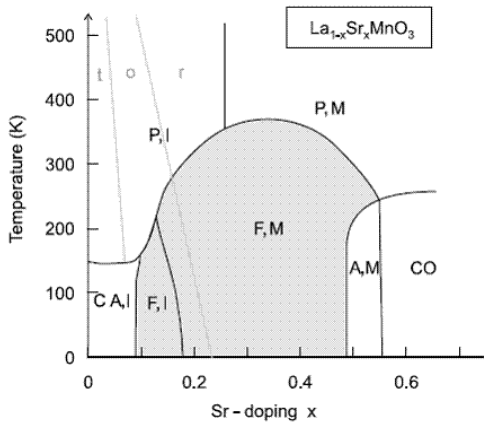

Figure 1.6: A phase diagram for LSMO. The magnetic phases are indicated by A (antiferromagnetic), CA (canted antiferromagnetic), F (ferromagnetic) and P (paramagnetic), CO marks charge ordered phases. The resistive behavior is denoted I (insulating) or M (metallic). In grey the structural phases are indicated by o (orthorhombic), r (rhombohedral) and t (tetragonal).

As can be observed it is extremely complex. The end compositions $REMnO_3$ ($x = 0$) and $AMnO_3$ ($x = 1$), with RE rare hearth and A alcaline metal are insulators at all temperatures and antiferromagnets at low temperatures. With a small doping ($x < 5\%$) a ferromagnetic phase can be obtained. Further doping ($x \sim 5-30\%$) results in a metallic phase and an increase of the magnetic transition temperature. Then close to $x = 0.5$, where the Mn^{4+} to Mn^{3+} ratio is about $1 : 1$, a charge-ordered (antiferromagnetic) insulating phase starts to evolve at low temperatures. The $La_{1-x}Sr_xMnO_3$ compound exhibits a structural transition from orthorhombic ($x \leq 0.2$) to rhombohedral ($x \geq 0.2$). The structural transition is modified not only by composition but also with temperature. In general the orthorhombic phase is stable at lower temperatures, while the rhombohedral phase requires higher temperatures. The $La_{0.7}Sr_{0.3}MnO_3$ compound, object of this work, is a FM, with a Curie temperature of about 370 K.

1.2.1 Colossal Magnetoresistance

The magneto resistance MR is dened as:

$$MR(H) = \frac{\rho(H) - \rho(0)}{\rho(0)} \tag{1.3}$$

where $\rho(H)$ and $\rho(0)$ represent the resistivity in presence and in absence of the external magnetic field, respectively.

In 1988 Baibich et al.[15] in Paris and Binasch et al. [16] in Juelich, independently one to each other, discovered that in certain multilayers exhibit a dramatic drop of the resistance when a magnetic eld is applied. Such effect was called Giant Magnetoresistance since it was bigger than had ever been previously observed in multilayers. For the manganite compounds doped with calcium an even bigger effect was discovered, which is referred to Colossal Magnetoresistance (CMR). In the case of $La_{0.7}Sr_{0.3}MnO_3$ the CMR is less relevant than in the case of $La_{0.7}Ca_{0.3}MnO_3$, exhibiting in presence of an applied magnetic eld H of few T a changing in the resistance of about 1 magnitude order.

In Figure 1.7 the resistivity as the function of temperature is shown for a strontium doped manganite oxide, for x=0.8.

The sharp drop of resistivity corresponds to the metal-ferromagnetic to insulating-paramagnetic transition occurring at a Curie temperature T_c near room temperature ([17], [18], [19]), that has been attributed to the strong coupling between the magnetic spin moments of the double valence Mn ions and electronic charge carriers.

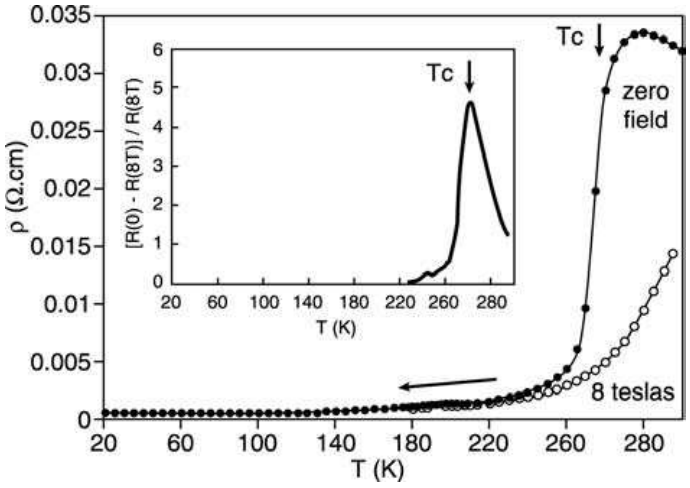

Figure 1.7: Resistivity in zero field in a 8T applied field versus temperature for $La_{0.8}Sr_{0.2}MnO_3$. In the inset, magnetoresistance ratio versus temperature. The array indicates the Curie temperature T_C

1.2.2 Half metals

The $La_{0.7}Sr_{0.3}MnO_3$ compound belongs to the class of the half–metal. Half metals are ferromagnets whose density of states in the conducting band shows only one occupied spin-polarized sub-band at the Fermi energy E_F (see Figure 1.8). The sub-band relative to the opposite spin orientation is completely empty, at least at low temperature, and separate by an energy gap.

If J and ΔE represent the difference in energy between such two bands and the band width, respectively, in the half metal compounds is $J > \Delta$E [20], [21]. As consequence, the current spin polarization value, defined as:

$$P = \frac{N_\uparrow(E_F) - N_\downarrow(E_F)}{N_\uparrow(E_F) + N_\downarrow(E_F)} \tag{1.4}$$

can be as high as 100%, at low temperature for the half metal compounds.

Half metallic ferromagnets, due to the highly spin-polarization of carriers, are ideal materials for spintronic. In this new field of the electronics, it is the spin orientation and not simply the charge of the carriers to transport the information. This is the reason why highly spin-polarized materials, such as $La_{0.7}Sr_{0.3}MnO_3$, are promising candidate for high efficiency spintronic devices.

The spin valve is the simplest magnetoresistive device. It consists of 2 ferromagnetic (FM) layers separated by a metallic (M) layer spacer. Each

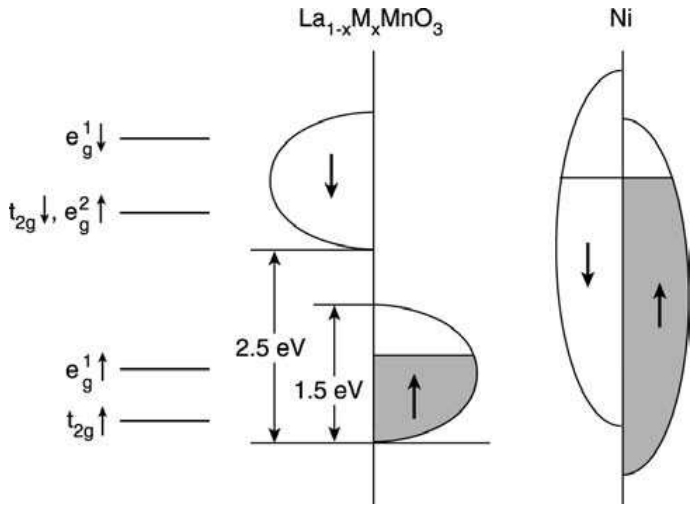

Figure 1.8: Schematic view of the electronic band structure of a $La_{1-x}M_xMnO_3$ compound. The level diagram on the left is that of an isolated Mn ion in an octahedral crystal field.

compound chosen for a FM layer exhibits different values of the coercive magnetic field. For a fixed value of an external magnetic field, one can assume a "pinned" magnetization for a layer, and a "free" magnetization for the other.

The free layer can switch between parallel and antiparallel alignments with the application of an external magnetic field.

The resistance of the junction depends on the spin orientation relative to an external magnetic field that can be parallel or antiparallel to the magnetization of the electrodes. The first case correspond to a low resistivity states, the second to a high resistivity state. A variant of the spin valve is the magnetic tunnel junction (MTJ) where the FM layers are separated by an insulator just a few atoms thick, shown as in Figure 1.9.

This device combines quantum tunnelling with magnetoresistance. In general a tunnel junction is formed by two metallic layers (electrodes) separated by a thin insulator layer (barrier); applying a bias voltage between two metal electrodes, an electrical current passes through the insulating barrier by quantum mechanical tunneling of the carriers. In the case of ferromagnetic electrodes, the tunneling process across the barrier is spin- dependent and the tunneling carriers can be spin-polarized.

According to Julliers expression, the TMR coefficient can be expressed as:

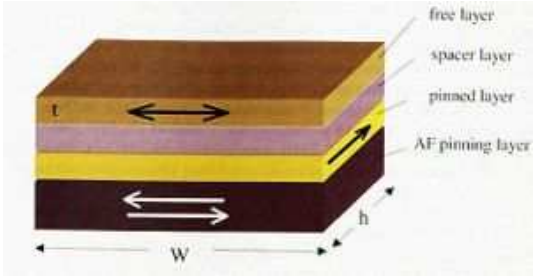

Figure 1.9: Schematic of a magnetic tunnel junction device.

$$\frac{\Delta R}{R} = \frac{R_{ap} - R_p}{R_p} = \frac{2P_1P_2}{1 - P_1P_2} \tag{1.5}$$

where R_p and R_{ap} are the resistance in the parallel and antiparallel state, respectively and P_1 and P_2 are the electron spin polarization of the two electrodes.

In order to develop high efficiency spintronic devices, highly spin-polarized current compound are needed, to enhance the TMR of magnetic tunnel junctions (active elements of MRAM), or to increase spin-polarization of currents injected into semiconductors.

For possible junction applications, the control of the growth condition is crucial, since in these materials the growth conditions strongly influence the transport and magnetic properties. Several groups have demonstrated the existence of large magnetoresistance at low fields in the doped manganites based on trilayer junctions. For example, Lu et al. [22] found that the shape and high intensity of MR ratio in trilayer junctions $La_{0.7}Sr_{0.3}MnO_3/SrTiO_3$ (exhibiting a large magnetoresistance at low fields) strongly depends on the quality of the LSMO/STO interface.

1.3 Strontium titanate $SrTiO_3$

The $SrTiO_3$ crystal has a cubic crystal structure with a tolerance factor of t$\sim$1.01, in which the Ti atom is embedded in the octahedron oxygen box and the Sr atoms occupy the cubic corners (see Figure 1.1).

The strontium titanate compound is often chosen as the substrate material in oxides thin films deposition, mainly for its chemical and compositional stability and for its lattice constant (3.905 $\AA$), well matched with the lattices parameters of a wide class of perovskites oxides compounds. The $SrTiO_3$

thus fits to be employed in the typically used high temperature deposition of heteroepitaxial oxides films.

Beside this wide utilization of $SrTiO_3$ as substrate, such perovskite shows several unexpected and sometimes ill undertood properties, that makes it a "case study". The $SrTiO_3$ is a transparent insulator, with an indirect energy gap of about 3.3 eV [23]. The conduction bands in $SrTiO_3$ correspond to the bands composed of mainly Titanium Ti 3d t_{2g} and e_g states, followed at higher energies by the bands of Strontium Sr 4d t_{2g} and e_g states. The upper valence band (UVB) contains 18 electrons in dominantly Oxygen O 2p states, hybridized with Ti and Sr states, and has a bandwidth of 5 eV. The interband transitions from the UVB to the Ti 3d bands and to the Sr 4d bands give rise to the transitions spanning from the indirect band gap energy of 3.3 eV up to 15 eV [28].

By modifying the $SrTiO_3$ compound chemically, this material can be made to show a wide variety of physical properties.

A dramatic effect on the transport properties of $SrTiO_3$ is exploited by electron doping, that can be achieved either by chemical substitution or by deviation from oxygen stoichiometry. In the first case, the most common n-type substitutions are lanthanum on the strontium site [29] and niobium on the titanium site [30], but different ones have also been successfully tried such as antimony on a titanium site [31].

In the second way, n-type doping of $SrTiO_3$ is obtained by creating oxygen vacancies, representing in a general sense a n-type dopants. This can be made in an easier way, with respect to the chemical substitution, simply by annealing the $SrTiO_3$ compound at high temperature in ultra high vacuum (about 950 °C in 10^{-9} mbar).

In presence of such oxygen deficiency it was observed that the $SrTiO_3$ compound turns from a transparent glittering to an opaque, black/dark blue material (see Figure 1.3)changing from insulating to conducting metallic [32] and exhibiting superconducting [33] transport properties. The superconducting behavior was discovered recently also in $SrTiO_3$ heterointerface with $LaAlO_3$, another dielectric perovskite insulator [34] and the measured value of the electrons mobility at the interface was found to be as high as 10^4 cm^2 V^{-1} s^{-1} at a temperature of 4.2 K.

Due to its wide extraordinary dielectric or transport properties, the strontium titanate $SrTiO_3$ is among the most used components in the perovskite oxides family compounds. Due to the tunably of the $SrTiO_3$ transport properties by introducing oxygen vacancies, some groups [35] tried to realize full-$SrTiO_3$ field effect heterostructures. The basic idea of such $SrTiO_3$-based device is to use a semiconducting or metallic oxygen decient $SrTiO_3$ as an

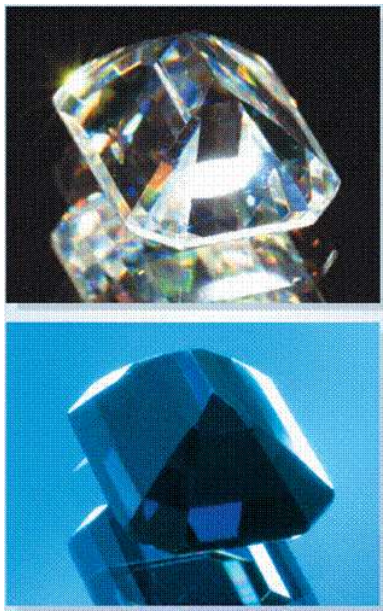

Figure 1.10: Two micrographs of a $SrTiO_3$ crystal show the effect of removing oxygen atoms, leaving vacancies in the crystal lattice: the glistening oxidized gem (top) is transformed into a dull blue,conductive crystal (bottom). The $SrTiO_3$ crystal, known as "*Lustigem*", was a popular diamond substitute in the 1960s.

active channel, and the stoichiometric insulating $SrTiO_3$ as an insulating layer for the gate voltage. Furthermore quantum paraelectricity, record-high permittivity (up to 10^4 at 10K) [36], ferroelectricity induced by compressive biaxial strain [37] or by isotopic substitution [38] observed in this compound open the way to promising technological applications.

Chapter 2

Experimental Set-up

The work was developed on an extremely complex experimental set-up called *MODA*, Modular facility for Oxides Deposition and Analysis. The system is a facility for pulsed laser deposition (PLD) of oxides thin films and analysis of their properties, by means of a very wide range of solid state and surface science techniques, such as RHEED, SPA-LEED, XPS, STM, AFM.

For the aim of my research activity, to the previously enumerated MODA tools was added a fast ICCD (Intensified Charge Couple Device) camera, for studying the expansion dynamics of the plasma produced by laser ablation during PLD process, by means of time gated photography technique.
Before starting my specific research activity, I was involved in the set-up of the whole MODA system, just arrived when I started the work.
After that, I focalized my attention on oxides thin film growth by PLD and on the two complementary techniques of time gated photography of ablated plasma and *in situ* RHEED of growing film.

Shortly, the ablation plasma was produced by focusing the output beam of a KrF excimer laser on stoichiometric $La_{0.7}Sr_{0.3}MnO_3$ and $SrTiO_3$ targets. During the experiments, the vacuum chamber was filled with oxygen gas. The substrate, attached on a metal holder, was positioned on a heater with the face parallel to the target. In the following I will refer to the heater temperature as the substrate or deposition temperature T_s.

The overall emission of the bright expanding plasma was recorded by means of fast ICCD camera, from the target laser ablation event, up to the arriving of the ablated species onto the substrate. By means of a high pressure RHEED, the deposition events was monitored, during the whole film deposition.
The details of the instrumentations and of the experimental techniques are described in the following sections.

2.1 MODA system

The MODA apparatus, shown in Figure 2.1 is a multichamber cluster system which allows to deposit oxide thin film by laser ablation and to analyze its as-grown uncontaminated surface by mean of several technique of analysis, after UHV transport ($< 10^{-10}$ mbar) through the characterization chambers. The fabrication of the thin film takes place in a vacuum chamber devoted to the pulsed laser deposition process (*PLD chamber*), evacuated up to a residual pressure of 10^{-9} mbar. A multitarget carousel situated in such chamber can allow the deposition of thin film multilayer or superlattices by using different targets, simply by changing the position of the target holder by means of a step motor. The analysis of the expanding plume produced during the pulsed laser ablation is performed by a fast ICCD camera, while the film deposition process is monitored *in situ* by a modified high pressure RHEED (Reflection High Energy Electron Diffraction). In the following the latter two techniques will be described in details. Once fabricated, the thin film is transferred toward the chambers devoted to the surface morphology analysis, by means of STM-AFM, SPA-LEED and XPS. All the techniques are briefly described in the following. The peculiarity of the MODA systems consist in the UHV connections (*load-locks*) between all the chambers of the system, that allows the analysis of the film surface properties avoiding any contamination.

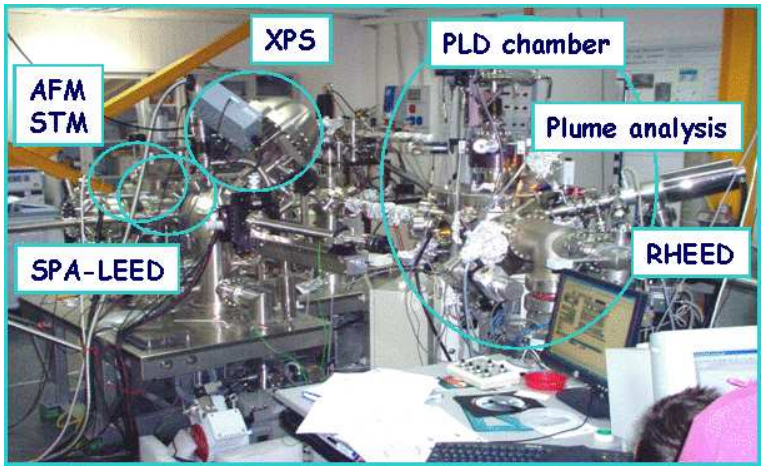

Figure 2.1: Photography of the MODA facility. Each instrumentation is highlighted by a label

2.2 PLD chamber

The multi-target holder and the substrate holder can be inserted in the deposition chamber (base pressure about 10^{-9} mbar) via a load-lock system without breaking the vacuum.

The heater is resistively heated using thermo-coax wires and the deposition temperature, read by a thermocouple, is controlled by means an electronic feedback system.
Depositions is performed in a fully software controlled mode. The degrees of freedom of the substrate holder, equipped with five independent software controlled stepper motors (XYZ-rotation stage, tilt angle θ and the azimuth angle ϕ), allow to vary at any time, even during the experiments, the positioning of the substrate in the plume. The pulsed laser deposition of complex oxides is performed using oxygen (99.999%) as deposition gas. The oxygen deposition pressure (10^6 – 1 mbar) is controlled by the effective pump speed and the total gas mass flow. The effective pump speed is adjusted through a variable restriction between the deposition chamber and turbo-molecular drag pump. The system is fully computer controlled including selection of the targets allowing for automated multi-layer deposition.

In the Figure 2.2 the top view image of the experimental set–up used in this work is shown.

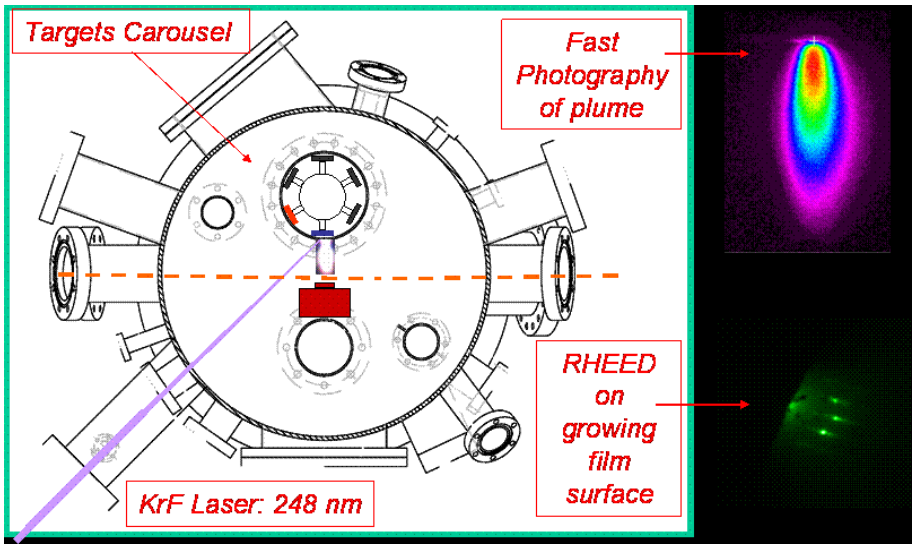

Figure 2.2: Top view of the deposition chamber and of the two diagnostic tools used for monitoring the plume expansion (ICCD camera) and the film growth (RHEED)

An KrF excimer laser (λ=248 nm, ≈25 ns full width half maximum, 2.0 J/cm^2, 45° angle of incidence) operated primarily at a repetition rate of 2 Hz, was used for $La_{0.7}Sr_{0.3}MnO_3$ and $SrTiO_3$ targets ablation. A mask is used to select the homogeneous part of the laser beam. The mask is projected at an inclination of 45° on the target by means of a focusing lens (focal length ∼ 50 mm). The energy density on the target is controlled by adjustment of, both, mask size and demagnification.

Each target was mounted on a rotating holder, to avoid drilling phenomena.

All films were deposited onto polished $SrTiO_3$(100) substrates (5 mm × 5 mm), attached with silver paste in the center of a large metal substrate holder, which was heated from the back side resistively and controlled at temperatures up to ≈1000 °C. Before performing the deposition, all the $SrTiO_3$ substrates were prepared with a combined chemical/thermal process to guarantee a single atomic termination. The target – substrate distance was fixed at d_{T-S} = 4.0 cm. The films were deposited at various substrate temperatures by adjusting the current applied to the resistive heating block, or at various oxygen pressures.

A fast ICCD camera was placed outside a deposition chamber flange, in order to perform time gated photography of the expanding plume. In the same time, with a second CCD camera the RHEED pattern spots intensity was recorded, during the film growth.

In the following sections, the details of time gated photography technique and of RHEED technique are explained.

2.3 ICCD–based Fast photography of the plume expansion

The plume expansion was observed by registering its bright plasma self-emission with a fast, intensified-charge-coupled-device ICCD (Andor Technology) equipped with a 1024 × 1024 array and operating in time-gated detection mode. A Nikon lens was used to image a 54×54 mm^2 region of the xz plane onto the ICCD camera to form a two-dimensional image of the plasma-plume self-emission. Each image was recorded by imaging the overall plume emission (in the spectral range of 350-900 nm) onto the ICCD, placed at right angles to the plume expansion direction, as shown in Figure 2.3.

To reduce the noise, a 2× binning was operated during image acquisition, obtaining a spatial resolution of ≈100 μm. Figure 2.4 shows an example of a plume image (upper panel) and the corresponding intensity profile along

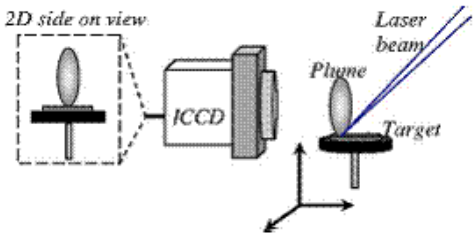

Figure 2.3: Schematic of the experimental setup used for the time-resolved imaging analysis by fast photography technique.

the normal to the target surface. From this analysis the plume front position R corresponding to each snapshots is estimated by evaluating the cumulative integral of the plume optical emission along the normal direction to the target.

ICCD gain and gate width were adjusted for each image in order to compensate for the reduction of the plume intensity during expansion. In particular, the following gate widths w were selected in order to have both a good accuracy of the plume dimension measurements and a reasonable signal-to-noise ratio, according to the time delay τ after the onset of plume: (a)w=5 ns for $0.1 \leq \tau \leq 0.5$ μs, (b) w =20 ns for $0.5 \leq \tau \leq 2$ μs, (c) w=50 ns for $2 \leq \tau \leq 5$ μs, and (d) w=100 ns for $\tau > 5$ μs. Therefore, the ratio between gate width and time delay (w/τ) is always less than a few percent, except for the first stages of the expansion where it is as high as 5%. For instance, in the acquisition interval (a), by considering the typical velocity of the plume front during expansion in high vacuum of 1×10^{-6} cm/s, we get an uncertainty of the plume front position of the order of ≈ 50 μm, which is indeed less than our spatial resolution. As the plume expands, the larger the time delay, the longer the plume dimension is, thus resulting in an uncertainty of the plume front position of less than 2% for the other acquisition conditions.

In an ambient atmosphere, the interaction with the background gas molecules produces a deceleration of the plume expansion with a consequent decrease of its extension at similar time delays after the laser pulse onset. This, finally, results in a plume front position uncertainty of the same order of that estimated above for high vacuum conditions. Therefore, we can safely use plume images to study the plume propagation dynamics in ambient atmosphere, reliably ascertaining interesting effects occurring at various times of the expansion and at different pressure levels.

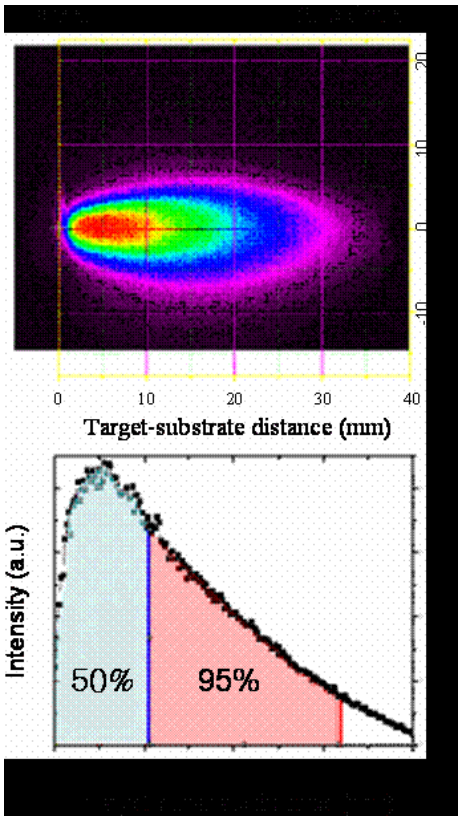

Figure 2.4: Example of ICCD acquisition: (up) $La_{0.7}Sr_{0.3}MnO_3$ plume 2100 ns after the laser shots, for oxygen deposition pressure of p=0.2 mbar. The white cross marks the arrival point of the laser shot onto target; (down) intensity emission cumulative integral along the direction normal to the target

2.4 RHEED: Reflection high-energy electrons diffraction

Reflection high-energy electrons diffraction (RHEED) technique utilizes diffraction of electrons by surface atoms to provide informations about the periodic rearrangement of the surface atoms.
In Figure 2.5 a schematic view of the used RHEED set-up geometry is showed. An high-energy electrons beam strikes the substrate surface at a grazing angle θ_i of 1-5°, which correspond to a penetration depth of only few atomic layers.

The component normal to the surface (k_{0z}) of the incident wave vector (k_0) determining the penetration depth into the material, can be varied sim-

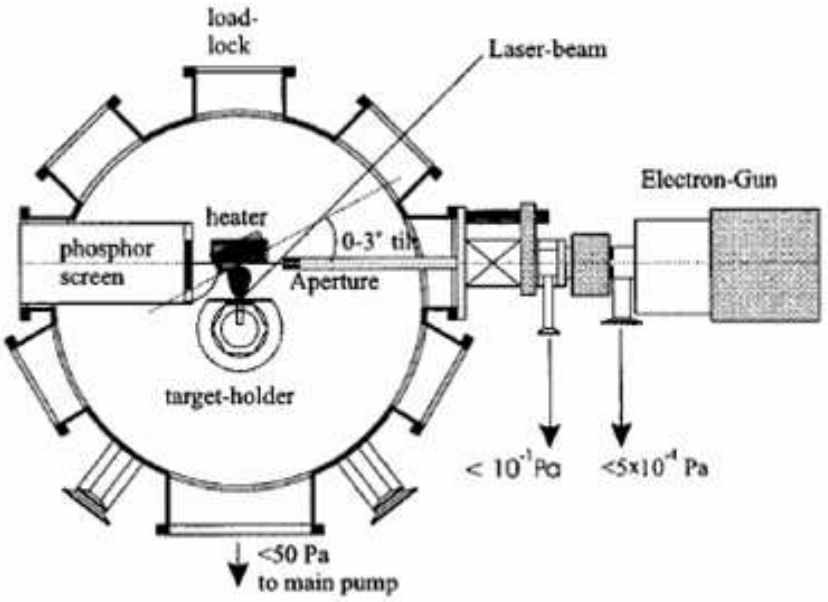

Figure 2.5: Top view of PLD chamber: RHEED experimental set-up

ply by changing the angle of incidence.

The electrons interact with the crystal potential and are scattered towards the phosphor screen displaying a characteristic diffraction pattern.

The electron gun (e-beam) and the phosphor screen are located far from the sample to avoid interference with deposition process. The beam convergence and the energy spread of the electrons determine the *coherence length*, which is the maximum distance between reflected electrons that are able to interfere. It's typical value is of the order of several hundreds nm [39].

The amplitude of the wave vector k_0 can be calculated as:

$$|k_0| = \frac{1}{\hbar}\sqrt{2m_0E + \frac{E^2}{c^2}} \tag{2.1}$$

where m_0 is the rest mass of the electrons.

The corresponding electron wavelength λ can be estimated by:

$$\lambda\left(\mathring{A}\right) = \sqrt{\frac{150}{E\,(eV)}} \tag{2.2}$$

neglecting the relativistic correction that represent only a few % for the typical energies value, ranging from 10 to 30 keV. With these energy values,

the electron wavelength λ is of about 0.05 – 0.1 $\mathring{A}$, which is an order of magnitude smaller then the thickness of an atomic layer [1].

These values of wavelength λ, together with a penetration depth of only few atomic layers, explains the RHEED high sensitivity to surface structure, making it a very powerful technique in surface science.

2.4.1 High pressure RHEED

With the typical pressure values used in oxides films deposition, it is not possible to use the "standard" RHEED system, due to its incompatibility with environmental pressure higher than 10^{-4} mbar.

In fact, the heated tungsten wire, used as electron source in the RHEED gun, requires an environmental pressure below 10^{-4} mbar to avoid breakage or a short lifetime. Furthermore, the electrons elastic and inelastic scattering with gas molecules gives rise to the attenuation of the e-beam intensity and, consequently, to very diffuse RHEED pattern, in presence of high deposition pressure. In order to overcome this problem, several groups tried to find alternative experimental conditions in RHEED-assisted pulsed laser deposition of oxides, for example working in low pressure condition of extremely oxidizing gases, such as ozone, NO_2, atomic oxygen or pulsed oxygen gas [24], [25], [26].

The limitation in using RHEED technique in high pressure oxides deposition was overcome introducing a two stage differentially pumped e-gun [44], that fulfilled both mentioned requirements: a low pressure in e-gun and minimum attenuation of e-beam intensity. Using this two-stage pumping system, the pressure in the deposition chamber can be increased up several tens of mbar, maintaining the vacuum (10^{-5} mbar) in the electron source. A schematic view of the two stage differentially pumped e-gun, used on MODA system is given in Figure 2.5.

The electron source is mounted on a flange connected to a stainless steel extension tube with an inner diameter of 8 μm. An aperture diameter with a diameter of 250 μm separates the tube from the deposition chamber. The XY deflection facility of the electron source is used to direct the electron beam through the aperture at the end of the tube.

The electron beam, which passes through the apertures inside the differential pumping unit and the tube, enters the deposition chamber near the substrate.

The fluorescent phosphor screen diameter 40 mm is mounted on a flange located near the substrate. The distance between the screen and substrate

[1] In our experimental conditions of 30 keV the value of λ is ~ 0.07 $\mathring{A}$.

is 40 mm. The screen is shielded from the plasma in order to minimize contamination.

The electron source, including the extension tube, is mounted on an XYZ stage allowing to adjust the distance between substrate and end of the tube. A minimum beam size of 100 μm can be obtained even at large working distances. The heater can be rotated in order to adjust the angle of incidence of the electron beam on the substrate. The azimuthal angle can be changed by additional rotation of the heater. The diffraction pattern is monitored by a charge coupled device CCD camera.

The attenuation of the e-beam intensity depends on the deposition pressure since the latter affects the mean free path of the electrons, L_E:

$$\frac{I}{I_0} = \exp\left(-\frac{l}{L_E}\right) \tag{2.3}$$

where l is the traveling distance of the electrons and I_0 is the e-beam intensity evaluated in the case of $l \ll L_E$, i.e. at sufficiently low pressure.

The mean free path L_E is defined as:

$$L_E = \frac{1}{\sigma_T n} \tag{2.4}$$

where σ_T is the total[2] cross section and n is the molecular density given by:

$$n = \frac{P}{k_B T} \tag{2.5}$$

with P the pressure, k_B Boltzman's constant and T the temperature.

2.4.2 Kinematic RHEED theory

Since the interaction of the electrons with the periodic potential of crystal is a strong, it could not be described quantitatively by a kinematic approach, which assumes only single elastic scattering events.

Nevertheless, this approach is widely used to both a physical understanding of the experimental RHEED results and to a qualitative description of the phenomena. For this reason, in the following a short description of the kinematic theory is depicted.

RHEED diffraction spots are produced when the momentum of the incident beam and that of the diffracted beam differ by a reciprocal lattice vector $\mathbf{G}$:

[2]due to both elastic and inelastic scattering

$$k_S - k_0 = G \tag{2.6}$$

where k_S and k_0 are the wave vectors of the diffracted and incident beams. A useful geometrical representation of the conditions of diffraction in elastic scattering, i.e., $|k_S|=|k_0|$, is given by the Ewald sphere construction, showed in the Figure 2.6.

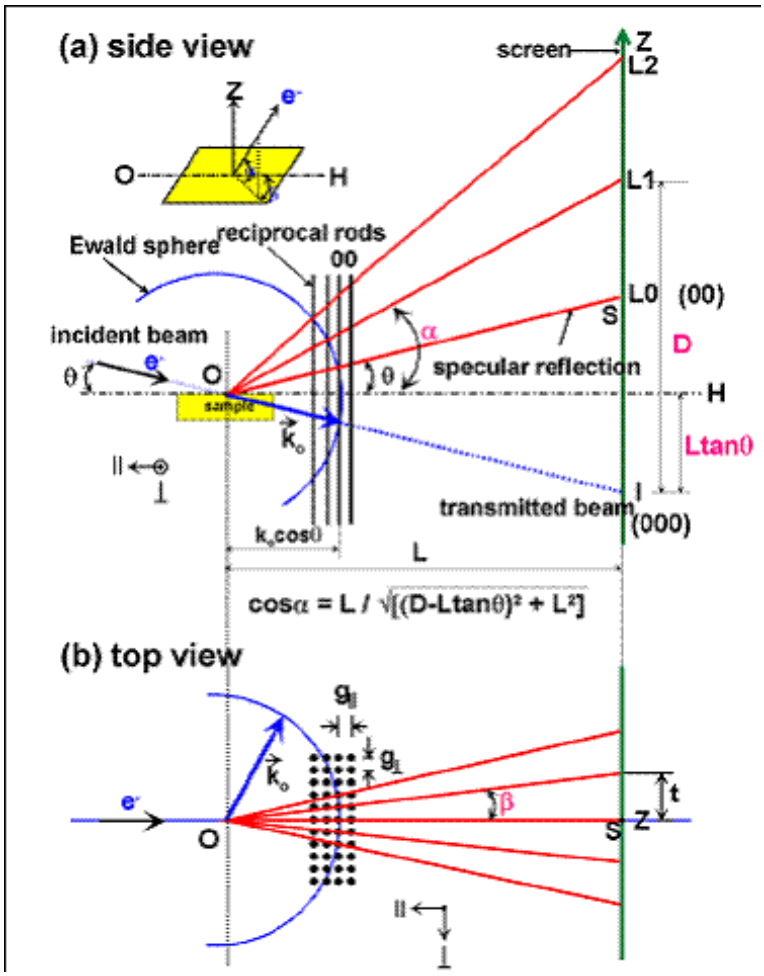

Figure 2.6: Ewald sphere construction in three dimension (a) and a section of the horizontal plane (b)

The reciprocal lattice of a 2D surface is a lattice of infinitely thin rods, perpendicular to the surface. The Ewald sphere construction can be done by drawing the tip of the incident wave vector attached to a reciprocal lattice

rod. The origin of this vector will be the center of a sphere with radius k_0 (equals $2\pi/\lambda$ for elastic scattering).

The reciprocal lattice rods intersecting the Ewald sphere will satisfy the diffraction condition in eq.2.6. In other words, the condition for diffraction is satisfied for all k_S connecting the origin of k_0 and a reciprocal lattice rod.

Due to the high electron energy used in RHEED, the radius of the Ewald sphere is very large compared to the reciprocal lattice spacing of sample crystal. As result, only few reciprocal lattice rods are intersected at the small grazing angle. Other areas of the reciprocal space are mapped by rotation of the sample about the incident angle (θ_i) or the azimuthal angle (ϕ_i).

In the case of a single-domain crystalline surface, clean and atomically flat[3], the diffraction pattern results in sharp spots lying on concentric circles, called Laue circles. Generally, we will refer our experimental data to the 0^{th} order Laue circle, i.e. to the intersections of the (0,k) rods with the Ewald sphere.

In presence of a three dimensional surface, as in the case of islands film growth, the RHEED diffraction pattern is a rectangular pattern of spots, due to the e–beam transmission trough small 3D features on the surface (as shown in Figure 2.7).

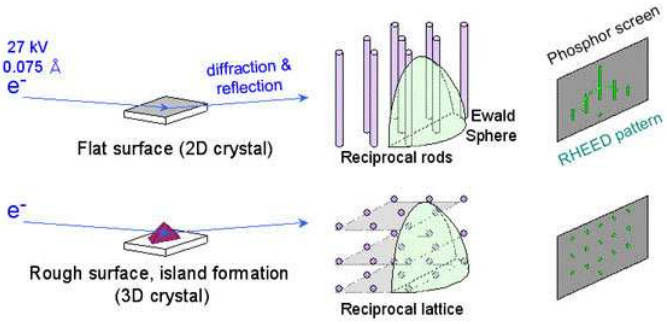

Figure 2.7: Example of RHEED pattern geometry for 2D and 3D surfaces.

Usually, due to the e-beam diameter and to the very small incident angle, the e-beam is not totally blocked and it reached the phosphor screen, appearing in the diffraction patter.

With a RHEED experimental set-up, two types of measurement can be performed: the study of the RHEED pattern of a well defined surface, before and after a deposition, or the analysis of the RHEED pattern spots intensity variation *during* the film growth.

[3]By now referred as perfect surface.

The RHEED patterns analysis provides a lot of surface information about surface reconstruction, degree of surface roughness, in-plane lattice parameters and strain.

Then, RHEED spots intensity variation provides informations regarding the kinetic of growth, such as growth mode and the growth rate on the monolayer scale, the diffusivity length of adatom on substrate surface, and film relaxation. In the following section 2.5, a detailed description of this kind of RHEED measurement is given.

2.4.3 Kikuchi lines origin

As mentioned before, the kinematic theory can not describe in an exhaustive way all the phenomena involved in the high energy electrons interaction with a crystal surface. The reason is that also dynamical scattering, neglected in this approach, should be taken into account, since RHEED is a *strong* interaction diffraction technique. For this reason, several "anomalous" phenomena are often observed in RHEED, as *Kikuchi lines*.

When the incident electron beam strikes the sample, in addition of elastic scattering, some inelastic scattering also occurs throughout the sample and in all directions. The energy loss in the inelastic scattering is small in comparison to the incident electron energy.

The inelastic scattered electrons may be oriented to the Bragg angle of other planes in the crystal and diffract off of them. The diffracted beams, whether they are directly or indirectly scattered from the incident electron beam, produce diffracted cones off of the planes which are diffracting (*Kossel cones*) which intersects the Ewald's sphere producing the *Kikuchi* lines.
The Kikuchi lines are actually curved, but due to the small wavelength of the electron beam the Bragg angles are small and the lines appear straight.

Kikuchi lines are interesting because of what they do when the crystal is moved in the beam. Diffraction spots fade or become brighter when the crystal is rotated or tilted, but stay in the same places; the Kikuchi lines move across the screen.

The difference in behavior can be explained by the position of the effective source of the electrons that are Bragg-scattered to produce the two phenomena. The diffraction spots are produced directly from the electron beam, which either hits or misses the Bragg angle for each plane; so the spot is either present or absent depending on the orientation of the crystal.

The source of the electrons that are Bragg-scattered to give Kikuchi lines is the set of inelastic scattering sites within the crystal. When the crystal is tilted the effective source of these inelastically scattered electrons is moved, but there are always still some electrons hitting a plane at the Bragg angle -

they merely emerge at an angle different to the one that they did before the crystal was tilted [40].

Kikuchi lines move rigidly fixed to the crystal and are, therefore, often used to determine the crystal orientation and for alignment of the e-beam. The occurrence of clear and sharp Kikuchi lines is an indication of a flat and crystalline surface.

2.5 In situ monitoring of growing film

One of the most interesting applications of the RHEED technique is the possibility to monitor the film growth dynamics by measuring the variation in intensity of RHEED spots pattern. Since 1981 it has become apparent that when growth is initiated, the intensity of RHEED spots shows changes that are directly related to film growth [41], [42]. Such application of RHEED technique has proven to be a very versatile tool to monitor the thin film growth by PLD [43] in presence of a specific two dimensional growth kinetics called *layer-by-layer* growth.

In such case the intensity of the RHEED pattern spots exhibits an oscillatory behavior, as sketched in the extremely simplified picture of Figure 2.8.

It is interesting to stress that, even if it is common to refer the RHEED oscillation data to the specular (0,0) spot of the diffraction pattern, the same oscillatory behavior is measured for the others spot, such as (0,1) and (0,-1).

The specular spot intensity variation is related to the changing in the surface roughness of the substrate during the film deposition. By introducing the coverage parameter θ, is possible to relate the RHEED intensity oscillation to the amount of new material arrived onto the surface for each laser ablation pulse.

For $\theta = 0.25$, some ad-atoms have arrived on the surface and islands are nucleated. The RHEED intensity decreases because of the decreasing of the reflectivity coefficient associated to the increased surface roughness. The intensity of the specular spot is minimum for θ=0.5, when the maximum surface roughness is realized. Then the intensity increases reaching a maximum when one monolayer of the film is completed (θ=1).

If the growth is purely layer by layer, the minimum and maximum intensities repeat in exactly the same way, with the same intensity, meaning that at each maximum the intensity of the specular spot assumes the same value taken after the completion of the first layer.
Usually, on the contrary, the average intensity of the specular spot decreases

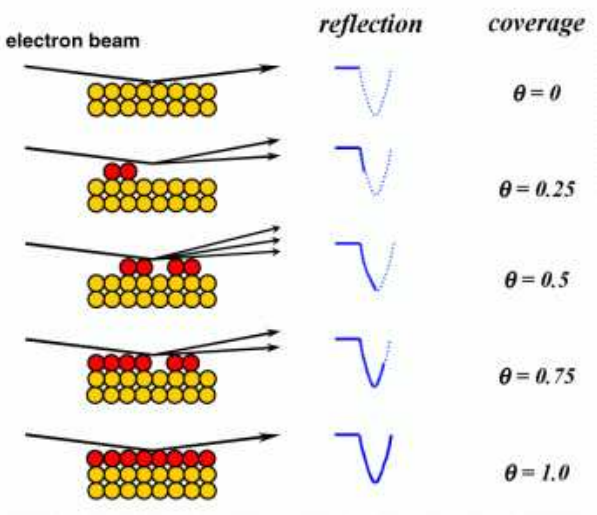

Figure 2.8: Example of RHEED intensity oscillations

by increasing the number of layers, an indication of a progressive roughening of the surface that it is common in the heteroepitaxial growth.

2.6 MODA analysis tools

2.6.1 LEED - Light Energy Electrons Diffraction

As in the case of RHEED, in LEED technique the pattern, displayed on a phosphor screen by scattered electrons, is an image of the reciprocal lattice of the investigated sample. Intensity maxima appear at those points in reciprocal space that fulfil the two-dimensional Laue conditions. The diffracted pattern thus reflects the symmetry of the surface unit cell, and the separation between the beams is inversely proportional to the interatomic distance.

The difference in LEED technique is in the energy of the monochromatic e-beam produced by an electrons gun: E_k ranges between 10 and 1000 eV. In such energy range, the electrons interact strongly with the substrate atoms and lose energy rapidly after penetrating into the crystal. In order to remove all diffracted electrons that have lost energy through inelastic scattering events with the sample atoms, a retarding field with spherical symmetry is created by applying voltages slightly lower than the primary beam energy to the grids situated in front of the screen. The electrons that overcome this retarding field are accelerated toward the phosphorescent screen, where

they produce bright spots whose intensity is proportional to the number of electrons in the corresponding beams.

2.6.2 XPS - X-ray Photoemission Spectroscopy

XPS spectroscopy makes it possible to precisely analyze the chemical nature of a given material by measuring the photoelectrons emitted from its surface.

From the analysis of such photoelectrons, the instrument produces a spectrum of emission intensity versue electron binding energy. Since the binding energies of the photoelectrons are characteristic of the element from which they are emanated, the spectra can be used for surface elemental ananlysis. Small shifts in the elemental binding energies provide information about the chemical state of the elements on the surface. The low kinetic energy (0 - 1500 eV) of such emitted photoelectrons limit the depth from which it can emerge so that XPS is a very surface-sensitive technique and the sample depth is in the range of few nanometers.

XPS measurements are performed in a third chamber of the MODA system, by employing a 5 channel hemispherical electron spectrometer and a dual anode (Mg and Al k - alfa lines) X-ray source. The general set up of the XPS system consists in an X-rays source emitting a beam that hits the sample, inducing the core-level electrons emission from its surface. Such photoelectrons are collected into an analyzer, by means of an electronic focusing system.

The analyzer, consisting in two hemispherical electrodes, allows a selection in energy of the photoelectrons. The potential difference between these two electrodes defines the path energy of the electrons. Only the electrons having a kinetic energy included in an interval of energy centered on this path energy will arrive at the detector. placed at the end of the analyzer. This multiplying detector (channeltron) produces a spectrum of emission intensity versus electron binding energy. In general, the binding energies of the photoelectrons are characteristic of the element from which they are emanated so that the spectra can be used for surface elemental analysis. Small shifts in the elemental binding energies provide information about the chemical state of the elements on the surface. Therefore, the high resolution XPS studies can provide the chemical state information of the surface.

2.6.3 STM- Scanning Tunnel Microscopy and AFM- Atomic Force Microscopy

Scanning tunnel microscopy (STM) and atomic force microscopy (AFM) techniques were both introduced by G. Binnig et al. [45] the first one in

1981, the second in 1986. In particular, STM was the first instrument to generate real space images of surfaces with atomic resolution.

Such techniques both allow obtaining high-resolution images of surface on an atomic scale, by means of a tip scanning the surface sample, but the used physical phenomena are different. The STM is based on the *tunnel effect*, while the AFM is based on the Van der Waals interatomic or electromagnetic forces. This is the reason why the STM technique can be used only on conductive solid samples, while the AFM can be employed on conductors, insulators, semiconductor, not only as solid surface, but also as liquid layers or liquid crystals.

In both microscopy techniques, the position of the scanning tip is controlled by means of piezoelectric transducers control the X, Y and Z directions.

The resolution in STM imaging is of 0.1 $\mathring{A}$ vertically and 1.0 $\mathring{A}$ laterally, while in AFM the vertical resolution is less then 1 $\mathring{A}$ and the lateral resolution $\sim$ 10 $\mathring{A}$. In both cases the lateral resolution depending upon the resolution of mechanical XYZ stage.

In STM, a small tungsten tip is positioned near a conducting sample. When a voltage is applied, electrons tunnel through the gap between sample and tip, generating a current that is extremely sensitive to the gap. In fact, since the tunneling current is exponentially dependent upon the distance between the tip and the sample, a small change in the distance between tip and sample corresponds to a large change in detected current. Typically, a feedback circuit is used to stabilize the current and maintain the tip at fixed distance from the sample. Beside this configuration of "fixed current", for STM measurements is sometime used the configuration of " fixed distance", in which the feedback circuit is disconnected. In this case, the morphology structure is obtained by the changing of the tunnel current during the scan. To avoid a tip crash on the higher structures of the sample, this second configuration is only used for small and atomically flat regions of the sample.

AFM operates by measuring attractive or repulsive forces between a tip and the sample. There are three ways to scan: (1)Contact Mode, with a direct physical contact with the sample, (2) Non-contact Mode: when tip oscillating at constant distance above sample surface, (3) Tapping mode, characterized by an intermittent contact between the tip and the surface, for a less damaging of the sample. In "contact mode", the AFM measures hard-sphere repulsion forces between the tip and sample. In non-contact mode, the AFM derives topographic images from measurements of attractive forces, but the tip does not touch the sample. In all the three AFM modality, the scanning tip is place at the end of an extremely flexible cantilever. During the tip scanning of the surface, the vertical deflection of the cantilever is

measured, generally by means of an optical lever. The optical lever operates by reflecting a laser beam off the cantilever. Angular deflection of the cantilever causes a twofold larger angular deflection of the laser beam. The reflected laser beam strikes a position- sensitive photodetector consisting of two side- by-side photodiodes. The difference between the two photodiode signals indicates the position of the laser spot on the detector and thus the angular deflection of the cantilever.

Because the cantilever-to-detector distance generally measures thousands of times the length of the cantilever, the optical lever greatly magnifies motions of the tip.

Chapter 3

Pulsed laser deposition

Although laser evaporation technique was first used to make thin films even in the 1960s [46], PLD was not rapidly developed until Venkatesan [47] and coworks successfully demonstrated in-situ preparation of $YBaCu_3O_7$ (YBCO) thin films by PLD technique during late 1987 and early 1988 [48], [49]. Since then, PLD has been widely used to prepare epitaxial thin films of any oxide materials. Pulsed laser deposition (PLD) is a physical vapor deposition technique based on the evaporation of material by means of a pulsed, highly energetic laser beam focussed onto the solid target by a lens. If the laser energy density is sufficient for ablation of the source target, the material evaporate, forming a gas plasma with the characteristic shape of a *plume*. This plasma plume expands along the direction normal to the target surface. When it reaches a substrate, placed in front of the target, a part of the evaporated material will form a thin film on this substrate.

The described PLD process can mainly be divided into four regimes: (i) the interaction of the laser beam with the target resulting in evaporation of the surface layers (evaporation regime), (ii) the interaction of the laser beam with the evaporated materials causing the formation of isothermal expanding plasma (isothermal regime), (iii) the anisotropic three-dimensional adiabatic expansion of the laser-induced plasma with a rapid transfer of thermal energy of the species in the plasma into kinetic energy, and (iv) thin film growth.

Due to the correlation between these physical mechanisms involved in PLD process, only an approximated description of the phenomenon is possible. This is the reason why it does not exist a theoretical model describing the whole PLD process. Instead, there exist several models, each of them analyzing in detail only one aspect of it, as the vaporization [50], the plasma formation [51], [52] and its expansion in vacuum [53], [54] or in presence of an ambient gas [55], [56].

In particular, plasma expansion dynamic, that plays a crucial role in

pulsed laser deposition, is not yet totally understood, even in the simpler case of propagation in vacuum. Furthermore, the expansion behavior is even more complex in presence of an eviromental gas, often used during PLD deposition of complex oxides.

In such case, additional physical processes affect the plume expansion behavior, such as plume deceleration and splitting, shock-wave formation, thermalization, etc. ([57], [60],[61]) as a consequence of plasma–background gas interaction.

In this section, the main aspects of the PLD process are described, from the initial laser-target interaction, up to the film nucleation and growth, when the plume reaches the substrate.

In particular, the attention will be focused on the plasma expansion dynamic, reporting two models widely used for describing this process in vacuum and in presence of ambient gas.

3.1 Laser ablation mechanisms

In PLD a pulsed high-energetic laser beam is focused on a target resulting in ablation of material. At the early stage of the laser pulse a dense layer of vapor is formed in front of the target. Energy absorption during the remainder of the laser pulse causes, both, pressure and temperature of this vapor to increase, resulting in partial ionization. This layer expands from the target surface due to the high pressure and forms the so-called plasma plume. During this expansion, internal thermal and ionization energies are converted into the kinetic energy (several hundreds eV) of the ablated particles.

Attenuation of the kinetic energy due to multiple collisions occurs during expansion into low- pressure background gas.

Usually, the laser ablation process is divided in two stages, separated in time:

1. target evaporation and plasma formation
2. plasma expansion

3.2 Laser target interaction

In an extremely simplified picture, the laser ablation of a solid target takes place when the local temperature, increased by means of the laser beam, overcome the vaporization temperature of such material. A number of parameters like the absorption coefficient and reflectivity of the target material,

and the pulse duration τ, wavelength λ and laser fluence F[1] affect the interaction of the laser beam with the target. Each material has its own threshold fluence F_{th}: for values of F above F_{th} the laser–target interaction regime is called ablation. For fluence values F lower than F_{th} the regime is called desorbing, for F higher than F_{th} it is called spallation.

From an analytical point of view, the problem of laser–target interaction is very complex: the presence of a moving laser-solid interface, resulting from the melting and the evaporation, and the thermal dependance of the sample optical and thermal properties on the temperature, make extremely complicated the exact description of the phenomenon.

For this reason it is widely used a macroscopic approach, based upon a energetic balance: the problem is transformed in the calculus of the temperature distribution on the sample, after the interaction with laser radiation.

The target region interested by the ablation process has the xy sizes of the laser spot dimension on target surface, times a L_{th} dimension, on the z direction perpendicular to the target. Such value of L_{th} depends on the thermal diffusivity of the sample material and on the pulse duration as followed:

$$L_{th} = \sqrt{2D\tau_L} \tag{3.1}$$

where D is the thermal diffusivity and τ_L is the pulse duration [62], [63], [64]. A can be seen, the longer the pulse, the deeper and the wider is the laser affected zone.

Since the value of L_{th} is usually very much smaller than the laser beam irradiated zone on the target surface[2], one can assume that the thermal gradient in the transverse plane xy of the target face is irrelevant with respect to the thermal gradient in z direction normal to the target. In this approximation, the temperature distribution $T(r,t)$ into the irradiated target is given by the one dimensional heat equation [62], [65], [66].

In general the interaction between the laser radiation and the solid material takes place through the absorption of photons by electrons of the atomic system. The absorbed energy causes electrons to be in excited states with high energy and as a result heat the material up to very high temperatures in a very short time. Then, the electron subsystem will transfer the energy to the lattice, by means of electron-phonon coupling.

In this frame, the temporal and spatial evolution of the electrons subsystem and the lattice should be described by means of two different temperatures: T_e (electrons) and T_i (lattice), on the base of the two temperature

[1] energy for pulse on spotsize

[2] with a ns laser pulse L_{th}= 1μm

diffusion model, developed by Anisimov et al. [67], [66], [68], [69], [70].

Nevertheless, in case of *ns* laser pulses, it can be assumed that T_e=T_i=T since the of electron–phonon coupling takes place on picosecond timescale (typically 1– 5 ps). With the previous approximation, the ablation process via a *ns* laser pulse can be described by the one dimensional heat equation in T:

$$C_i \frac{\partial T}{\partial t} = \frac{\partial}{\partial z}\left(k_0 \frac{\partial T}{\partial z}\right) + \alpha A I\left(t\right) e^{-\alpha z} \tag{3.2}$$

where C_i is the heat capacitance of the lattice, $I(t)$ is the laser pulse intensity, k_0 is thermal conductivity and α is the absorption coefficient.

3.3 Laser–Plasma interaction

In the description of the laser–plasma interaction, the laser pulse duration plays a crucial role: whereas in the case of nanosecond (ns) laser pulse[3], the forming plasma interacts with the laser beam "tail", in the case of femtosecond (fs) laser pulse the previous mechanism doesn't take place.

The laser absorption of the forming plasma reduces the efficiency of the energy deposition into the sample (*plasma shielding* effect) and increases the plume ionization degree, complicating the plume expansion mechanism. Due to the plasma-laser interaction, the temperature of the evaporated material increases therefore rapidly to extremely high values and the electrons are further accelerated. The excited particles will emit photons, leading to a bright plasma plume, which is characteristic for the laser ablation process. The main absorption processes are the *inverse bremsstrahlung* (IB) and the photoionization (PI), since the cross section of the other processes are much smaller [71], [65], [72].

3.4 Plasma plume expansion

Since the onset of the material removal described in the previous sections takes place within a very short time after the pulse (1-100 ps), on the time scale of the plasma expansion (μs) the laser–target event can be regarded as a momentary release of energy.

The spatial structure of the vapor plasma at the early stage of its expansion is well known to be a cloud strongly forwarded in the direction normal to the ablated target. The reason of this characteristic plasma elliptic shape,

[3] as our experimental case

called *plume*, is in the strong difference in pressure gradients in axial and radial directions: the plasma expands in the direction of maximum pressure gradient.

Among the several models dealing with plume expansion, a first distinction should be done between plume expansion in vacuum and in an environmental gas. In the following, some approaches to the description of the plume expansion in a vacuum as well as into a background atmosphere will be briefly illustrated. The plume expansion dynamic in vacuum was extensively investigated by Anisimov et al. [53] and by Singh and Narayan [54], resorting to a self-similar expansion of an elliptical, neutral gas cloud.

The two previous cited models differ essentially for the analysis of the plume expansion during the first stage, which timescale is of the order of the laser pulse duration. Then, after the laser pulse, both models hypothesize an adiabatically expanding plume, in which the plume energy, initially purely thermal, is progressively transformed into kinetic energy during the expansion. After a short transient stage, the plume front dynamics becomes linear with respect to time, reaching a maximum, asymptotic expansion velocity. This free-plume expansion stage is reached when all the initial thermal energy has been transferred to kinetic energy of the ablated species, which travel at the asymptotic velocity during the further expansion. These models describes pretty well the angular distribution of the ablated material as well as the thickness profiles of the deposited films.

In the case of expansion into an ambient atmosphere, the plume acts as a piston compressing the background gas during its expansion. As a consequence of this interaction, plume expansion along the direction normal to the target surface is braked to some extent, and the plume shape tends to be more and more hemispherical. For the sake of simplification, the theoretical analysis of plume propagation into an ambient gas is usually modeled for the case of a hemispherical plume.

Among the plume expansion models in gas [**?**] [56], [55] and [60], here we will shortly recall those developed by Predtechensky [56] and Arnold [55]. In both these models, the ablated materials act to sweep up the environmental gas, driving it at supersonic velocity. As consequence, a contact front is formed between the plume and the ambient gas. While the former only deals with the dynamics of the contact front, the latter also considers the internal dynamics of the plume and of the external background gas layer formed during plume-ambient gas interaction.

In the initial stage of the expansion, the plume mass is large compared with the mass of the driven gas accumulated at plume front. For this reason, the early stage of the plume expansion in gas does not significantly differ from the expansion in vacuum. This hypothesis is confirmed by several ex-

perimental measurements, showing a initial plume front velocity value very close to that observed in a vacuum (10^6 cm s^{-1}) [73], [53], [74].

During the plume expansion, the gas adjoint mass on the plume front increases. The mass of the plume and the adjoint background mass swept away during the propagation, are considered confined into an hemispherical thin layer at the plume front. The Predtechensky et al. and the Arnold et al. models differs in their basic hypothesis and physical assumption.

The approach used in the he Predtechensky and Mayorov model describes the dynamics of the front expansion of a plume into a background gas considering an hemispherical plume expansion, as schematically shown in figure Figure 3.1.

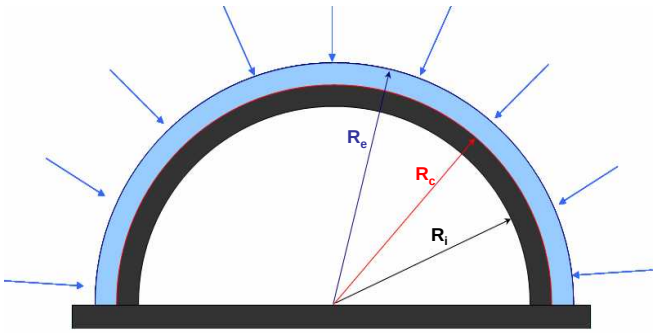

Figure 3.1: Sketch of the Predtechensky and Mayorov plume gas interaction model: the boundary of the plasma plume R_i, of the external shock wave R_e and of the contact front R are shown.

This model considers the balance between the linear momentum Q of the total mass (i.e. plume and adjoint background gas) confined into an infinitely thin layer at a distance R from the centre O and the force F acting at the periphery of the hemispherical thin layer due to the background gas pressure p_0. Here the boundary of the plasma plume R_i, of the external shock wave R_e and of the contact front R are equal, i.e. $R_i = R_e = R$.

The progressive increase of the background mass at the plume periphery leads to a gradual reduction of the plume front expansion velocity, until a

stopping stage is finally reached.

Even using a simple physical approach, which does describe the basic influence of the background gas on the plume dynamics, the model allows its applications in different cases without requiring complex numerical methods and calculations. Due to these features, we will rest on this model in our analysis of the experimental results and, for the sake of easiness we will present it in complete form in the section 4.3.

Contrary to Predtechensky and Mayorov model, Arnold et al. [55] developed a more complete model, which takes into account also the processes involved in plume-background gas interaction affecting to the plume internal structure. In such model, the description of the expansion dynamics of an hemispherical plume is based on the laws of mass, energy and momentum conservation.
The segmentation of the plasma in the spherical expansion in Arnold's model is schematically presented in Figure 3.2.

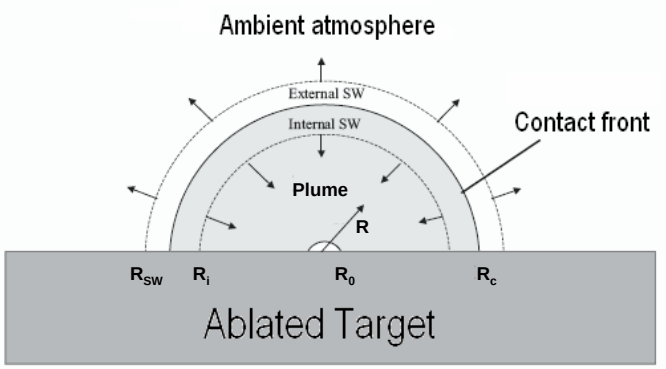

Figure 3.2: A scheme of the plume in the Arnold et al. expansion model. R_0 is the initial radius of the plume. The contact front between the plume and the ambient (R_c) is moving with the velocity $R_C^{'}$. (R_{SW}) denotes the front of the external shock wave propagating in ambient gas. The internal shock wave (R_i) propagates inwards, to the center of the plume.

This model refers to two region in contact: one on the edge of the traveling plume (with radius R_c) and the other in the ambient gas along the plume periphery (with radius R_{SW}). During the plume expansion, the ablated particles and the ambient gas molecules are confined and compressed in two thin

layers, due to the reciprocal interaction. Because of the collisions that take place in such two thin layers in contact, deviations from the free expansion will occur.

When the adjoint mass of the gas in the external layers is comparable to or bigger than the mass of the ablated species confined in the thin layer on the plume edge, the plume expansion velocity starts to slow down. As consequence, high counter–pressure builds up in the ablated material near to the contact front (R_C).

In that region, the gas temperature is raised as the plume molecules collide with those of the gas and become reflected. The density is higher than in the center of the plume, giving rise to the so called *snowplough effect*. The internal shock wave (R_i) formed in such a way propagates inwards. A significant part of the plume energy becomes thermal as the internal shock wave reaches the center. Much weakened, it is reflected and the plume homogenizes. Mixing of the plume and the ambient gas is not treated by the model.

The model considers the redistribution of energy between the thermal and kinetic energies of the plume and the shock waves. Equations for four dynamic variables R_i, R_{SW}, R_C, and R are formulated from the conservation laws derived from gas dynamics [55].

The models equation states that the amount of compressed gas in the external shock wave (mass in the layer between R_C and R_{SW}) is equal to the amount of ambient gas that is repulsed by the plume. The overall energy conservation states that the total energy in the plasma, i.e. the laser energy minus losses due to reflection, heat diffusion, plasma radiation, etc., is equal to the kinetic (E_k) and thermal (E_t) energies in the different parts of the plasma.

Assuming a spatially homogeneous pressure within the shock waves, the thermal energies E_{i_t} and E_{SW} are determined by p_C which is the pressure at the contact surface in the semi-spheres of the shock waves. p_C can be obtained from Newton's law describing the balance of forces for the external shock wave:

$$\frac{d}{dt}\left[P_{SW}(R_C, R_{SW}, R'_C, R'_{SW})\right] = 4\pi R_C^2 \rho_C - 4\pi R_S^2 W p_{amb} \tag{3.3}$$

P_{SW} denotes the momentum of the shock wave which also has to be estimated. With the appropriate initial conditions, these equations can be solved numerically.

For different stages of the plasma expansion, approximated solutions exist. The temporal behavior of radii R_i, R_C, R_{SW}, and R obtained from such a

numerical calculation is plotted in Figure ??. in a dimensionless presentation [55].

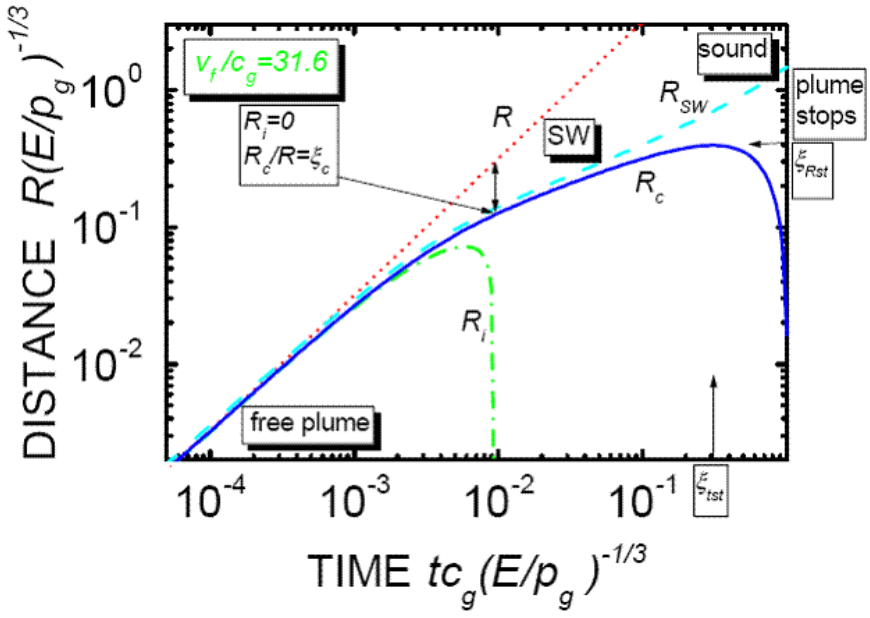

Figure 3.3: Dynamics of plume expansion in dimensionless variables (from [29]). Dotted line: free plume R; dash-dotted line: internal SW R_i; dashed line: external SW R_{SW}; solid line: contact boundary R_C. v_f is the free plume expansion velocity and c_g the sound velocity in given medium.

At the earliest times, the plume evolution does not differ from the free expansion in vacuum, the plume deceleration can be seen from the increasing difference between R_C and R. The decrease of the radius R_i marks the moment in which the internal shock wave reaches the center. Its further reflections are not treated by the model, and the plume is considered to be homogeneous after that. Providing the external shock wave is strong enough, the plume will be stopped and the contact front radius R_C will not grow further. At that point, the validity of the model becomes limited since effects like diffusion become significant. In fact, it has been observed that a small fraction of plume species can still reach a substrate located at distance larger then the stopping distance, and it has been proposed that this is due to diffusion [75]. The time scale of the expansion depends strongly on the total energy of the plume and the ambient pressure.

Despite the theoretical predictions on plume expansion behavior of such

model matched pretty well with experimental results of plume expansion, due to its complexity it does not allow to take into account complicate effects. For this reason, while we referred to this model to interpret our experimental results of the gas ambient pressure effects on the plume expansion [73], for the here presented study regarding the effect on plume expansion dynamic of deposition temperature, we will refer the Predtechensky et Mayorov model. The effect we observed of deposition temperature on gas ambient, inducing a change on its density profile, was impossible to take into account in Arnold's model.

3.5 Plume-substrate interaction

In PLD, the deposition of the ablated material on the substrate surface can be regarded as instantaneous for every pulse, since the time scale of the atomistic processes involved in the film growth exceeds the deposition pulse duration. Each instantaneous deposition is followed by a relative long time interval, where no deposition takes place. Because of the instantaneous deposition at typical PLD conditions, the nucleation takes place after the deposition pulse and can be considered as post- nucleation.
Such separated random deposition and subsequent growth is, furthermore, advantageous for the study of the effect of plume expansion dynamics on film growth kinetics developed in this work.
Parameters which control the instantaneous deposition rate are the laser energy density at the target, the distance between target and the substrate and ambient gas properties, i.e., pressure and mass.

The extremely high deposition rate, typical of PLD deposition (of the order of 10^{20} atoms cm^{-2} s^{-1} [39], [76]), leads to a very high degree of supersaturation, $\Delta\mu$, defined as:

$$\Delta\mu = k_B T \ln \frac{R}{R_0} \tag{3.4}$$

where k_B is the Boltzmann's constant, R is the actual deposition rate and R_0 its equilibrium value at temperature T.

Two independent process play a role during the vapor-phase epitaxial growth on a surface: the nucleation and the growth of islands. Both processes take place far from the thermodynamic equilibrium and are determined by kinetic processes. In the frame of the thermodynamical approach, used to describe the crystal growth close to equilibrium[4], local fluctuation from

[4]for a thermodynamically stable system

equilibrium leads to the the phase transition from gas to solid, where a prerequisite for this process of *nucleation* is a supersaturated gas.

The high supersaturation of the vapor leads to a large nucleation rate. The nuclei will be formed until a critical density is reached. From this point onwards the nuclei will grow and *crystallization* process will take place.

3.6 Film growth modes

In the following a schematization of the possible ways of growth, determined by the thermodynamic approach of the balance between the free energies of film (γ_F) and substrate (γ_S) and the interface between film and substrate (γ_I) is given.

When the total free energy of the film surface and the interface equals the free energy of the substrate surface ($\gamma_F + \gamma_I < \gamma_S$), significant wetting is expected. This leads to *layer-by-layer* growth as described by Frank and Van der Merwe [77].

In the case of an increased total free energy wetting is energetically unfavorable and the deposit will take place minimizing the film substrate interface by means of islands growth; this is the case of *Volmer-Weber* mechanism [78], where the energy due to the creation of interface is higher than the surface energy of the substrate and film ($\gamma_F + \gamma_I > \gamma_S$).

At the intermediate case, a transition from the Frank and Van der Merwe to the Volmer-Weber growth mode can be observed. Here a crucial role is played by the mismatch between film and substrate, inducing a strain on the growing film. A layer-by-layer growth take place in the first stage. Then, the thicker become the film, the higher is the elastic energy due to the strain. Such large strain energy can be lowered by forming islands in which strain is relaxed. This mechanism results in a continuous film of one or two monolayers onto which successively discrete islands are formed. This way of growth is the so-called Stranski-Krastanov [79].
In the Figure 3.4, the previous regimes are depicted.

The previous approach doesn't take into account the effect on the growth kinetic of the deposition parameters, such as the value of supersaturation in the gas phase, the substrate vicinality[5] and the crystallographic misfit between the film and substrate unit cells.

For the effect of such parameters, different growth modes have been observed for the same film-substrate system, thus clearly indicating that growth techniques and parameters are crucial to determine the final film morphology.

[5]the miscut between the substrate surface and the ideal crystallographic plane

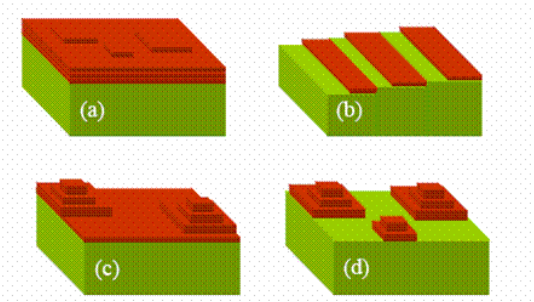

Figure 3.4: Film possible growths: (a) Frank-Van der Merwe or *layer-by-layer* growth, (b) *step-flow* growth (described in the following), (c) Stranski-Krastanov growth, (d) Volmer-Weber growth.

A first difference should be done between *homoepitaxy* and *heteroepitaxy*. In the first case the film and substrate compounds are the same deposited and the substrate crystalline structure extends into the film during the growth.

In case of heteroepitaxy, the materials of film and substrate are different, with different lattice parameters. Such lattice mismatch gives rise to a strain, tensile or compressive, that can be calculated as the ratio between the lattice parameters of the substrate and bulk/film:

$$\delta = \frac{a_s - a_f}{a_f} \tag{3.5}$$

where a_s and a_f are the unstrained crystal bulk lattice parameters in plane of film and substrate. In general the strain can be elastic, and in this case a deformation of the in plane lattice parameters produce an out of plane deformation of the cell in order to conserve the volume. If $a_{sub} > a_{bulk-film}$, $\delta > 0$ imply tensile strain on the deposited film in plane, and out of plane compressed, while for $\delta < 0$ the strain is compressive and in plane lattice is compressed, but expanded out of plane. In the case of thin film deposition of $La_{0.7}Sr_{0.3}MnO_3$ on $SrTiO_3$ (where a_0=0.3873 nm for $La_{0.7}Sr_{0.3}MnO_3$, and a_0=0.3905 nm for $SrTiO_3$), the strain is tensile, of about 0.8%, as showed in Figure 3.5.

The effect of this strain on the growing film results in an elastic energy that increase with increasing the film thickness. When the thickness exceeds a so-called *critical thickness* (h_C), the accumulated elastic energy becomes comparable with the interfacial energy, and the strained film tends to relax by creating misfit dislocations near the film-substrate interface. In heteroepitaxy, the misfit usually induces Volmer-Weber growth, except for

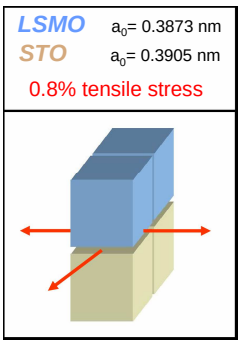

Figure 3.5: Tensile strain in $La_{0.7}Sr_{0.3}MnO_3$ thin film on $SrTiO_3$

large interface energies between substrate and deposited film, which cause the Stranski-Krastanov growth.

The substrate vicinality provides terrace surface, separated by steps. The steps heights and the terraces length depend on the angle and the direction of the miscut. On a vicinal substrate, beside the growth modes described above, a fourth way of growth can occur: the *step-flow* mode (see panel (b) in Figure 3.4). This growth mode takes place on vicinal surface with high steps density and small terraces, in some deposition condition. In this case, the steps act as a sink: the adatoms diffuse towards the substrate steps preventing the nucleation on the terraces. As result, steps will propagate during the growth. Since the diffusing adatoms attach to the step edges, the result is the advancement of the steps of the substrate surface. This growing mode will go on indefinitely, with no changes in the starting substrate surface morphology, if both the terraces will keep the same width and the step ledges remain straight. Otherwise, step bunching can occur: in this case a high density of steps moves with large velocities over the growth surface. By fluctuation, higher steps catch up with lower ones and then move together as double, triple steps. Subsequently, the distribution in the terrace length (l_T) broadens [76].

3.6.1 Growth kinetics

For the sake of simplicity, in the following it will be discussed the growth kinetics in the homoepitaxy case, where complicating effects as lattice parameter misfit and thermal coefficient expansion do not play a role.

Once adsorbed on the surface an atom, now called *adatom*, may desorb into the vapor or change adsorption site, in which case it can diffuse on the

surface for several atomic length, before to be detached and incorporated in the crystal structure, as schematized in Figure 3.6.

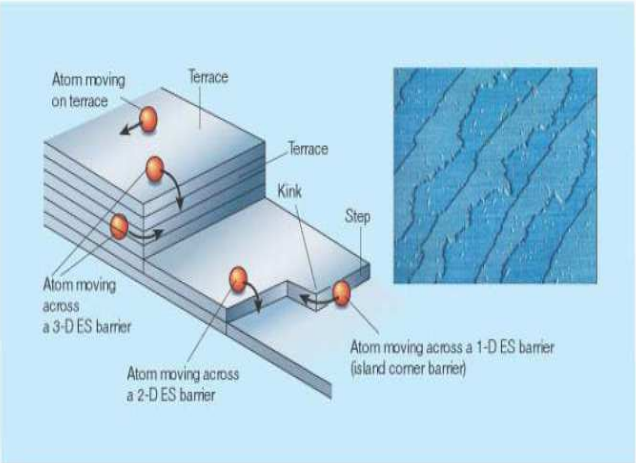

Figure 3.6: Adatoms kinetics schematization

The molecule-surface interaction is described by a potential that is a periodic function of the two coordinates parallel to the surface and a decreasing function of a third coordinate normal to it.

If l_T is the terrace length, we define l_D as the average distance an atom can travel on a flat surface before being trapped. It is given by:

$$l_D = \sqrt{D_s \tau} \tag{3.6}$$

where (D_s) is the surface diffusion coefficient of the adatoms, and τ is the residence time before re-evaporation.

The surface diffusion coefficient D_S[6] is generally expressed as:

$$D_S = a^2 \nu \exp\left(-\frac{E_A}{k_B T}\right) \tag{3.7}$$

where E_A is the activation energy for diffusion, a is the characteristic jump distance and ν is the *sticking coefficient*. The sticking coefficient expresses the probability of a molecule to be captured, once impacting on the substrate

[6]typical values for metal oxides lie between 10^{-4} and 10^{-8} cm^2 s^{-1} [39]

surface, and it is given by the ratio of the captured molecules to the total number of molecule hitting the surface.

From the equation (3.7) it became evident the importance of the deposition temperature in the PLD technique, since it controls, among others, the diffusivity of the adatoms. However, is important to recall here that the adatoms mobility on the surface is determined not only by the deposition temperature. An important contribute in the nucleation process come from the redistribution of the kinetic energy of the incoming flux of impinging atoms.

The diffusion process is a crucial phenomenon that determine how the deposited materials rearrange itself on the surface and by a careful control of these parameters it is possible to obtain 2D growth modes not only on singular, but also on vicinal substrates. To understand this, two diffusion process have to be considered, both determined by kinetic parameters [39]:

1. The intralayer mass transport: the diffusion of atoms on terrace
2. The interlayer mass transport: the diffusion of atoms to a lower step[7]

In the case of fast intralayer mass transport, the mobility of the adatoms is high enough to enable atoms to reach the edges of the substrate steps, i.e. the diffusion length l_D is larger than l_T, the average terrace width. In this way the nucleation on the terraces is prevented and the *step-flow* growth takes place.
Even on a vicinal substrate, a 2D growth will occur, until $l_D > l_T$. Otherwise, if for some reason the distribution in l_T of the surface broadens, nucleation on the terraces will occur. When this happens, nuclei will form until a saturation density is reached. After that, the probability for atoms to attach to an existing nucleus exceeds the probability to form a new nucleus and so islands will start to grow. In this case the interlayer mass transport plays a big role to determine the growth mode. In fact, to obtain a layer-by-layer growth mode in this situation, a steady interlayer mass transport should be present so that atoms deposited on top of a growing island must reach the island edge and then diffuse to a lower layer. In the ideal case, the nucleation start after completion of a layer. But if there is no interlayer mass transport, nucleation will occur on top of islands before these have coalesced and this is the case of the so called second layer nucleation. The probability for second layer nucleation is related to the mean island radius at the time of stable clusters nucleation on top of the islands, R_C. The value of R_C is, in turn, related to the parameter E_S, that is the energy barrier for an atom to descend

[7] diffusion to a higher terrace is usually neglected.

across the step edge to a lower terrace. Larger is the value of E_S, smaller will be the value of R_C, since the additional[8] energy barrier lead to accumulation of the adatoms on top of the islands, with subsequently increase of second layer nucleation rate.

In the real system the growth mode is in between these growth modes described here. In some cases, even a transition from a layer-by-layer to a step flow growth on vicinal substrate can happen when the diffusion length of adatoms becomes comparable to the terrace width, i.e. when $l_D \approx l_T$. This can happen because either the substrate temperature, determining the surface diffusion length l_D or the vicinal angle, determining the terrace width l_T, is changed.

3.6.2 RHEED oscillations models

Even with the ever increasing RHEED observations accumulated and with the comparison between experimental RHEED data on the epitaxial growth of various materials with theoretical prediction, a still open question is what does really RHEED measure and what is the origin of the observed oscillations. Essentially, there are two models for explaining the RHEED intensity oscillations during film growth.

One is based on a two level interference model in which the incremental monolayer *coverage* is responsible for the oscillations. This model leads naturally to attributing the RHEED oscillations directly to a 2D layer-by-layer growth.

The other relies on the concept of *step density* on the analyzed surface, postulate that the step edges dominate the scattering of the electron beam [80]. In the frame of the step density model [81], [82], widely used for the very good agreement with experimental data [39], each laser pulse changes the step density on the substrate surface. In the hypothesis of an instantaneous nucleation [9] the step density S can be defined by:

$$S = 2\sqrt{\pi N_S}(1-\theta)\sqrt{-\ln(1-\theta)} \tag{3.8}$$

where N_S is the number of nuclei for unit area and θ is coverage of the surface. Both diffusivity of the deposited material and the deposition rate determine the quantity N_S and therefore the amplitude of the step oscillations.

[8] The other energy barrier has been defined as E_A, see (3.7)

[9] This hypothesis is valid for PLD, because of the high supersaturation within the deposition pulse

Experimentally, is well known that the RHEED intensities are modulated by the laser pulse, giving rise to the typical RHEED relaxations [83],[84]. Following the previous model, i.e. in the hypothesis of an instantaneous nucleation just after the laser pulse, this relaxation behavior is attributed to particles diffusing towards the step edges of the islands, with sequent increase of the islands size. As a consequence, the step density of the surface changes. The evolution of the step density after every pulse is, therefore, a direct result of the decay of the density of the diffusing particles, which depends on the diffusivity and on the average travel distance, see the eq. [**?**]. This distance is determined by the nucleation density N_S and by the average islands size.

In the frame of the step density model, the RHEED intensity variation during the film growth is due to the electrons - step edges scattering (remembering that the unit cell layer thickness is much larger than e-beam wavelength). That is, the change in RHEED spots intensity is a measurement of the substrate surface step density.

In the Figure 3.7 a schematic example of the experimental results of specular spot intensity measurements during film deposition is depicted, for the different film growth modes. The step density model successfully explains the experimental behavior.

From the step density model, the RHEED intensity is expected to exhibit an oscillatory behavior, because of the periodic changing in step density of the surface during the film deposition. The increased value of step density after each laser spot, decrease by means of coalescence mechanism of the growing islands. The minimum in specular RHEED intensity correspond to the maximum step density, when the scattering angle of the electrons is wider, due the higher degree of "disorder" of the surface. Sometimes, during a layer-by-layer growth the formation of an island on the surface can occur, before the layer is completed. In this case the oscillatory RHEED signal shows a *dumping* in the intensity [39].

In the case of 3D growth mode, the step density on the surface increases in time and subsequently the specular RHEED intensity will decrease, due the increased step edges scattering the electrons in all directions.

In the case of a step-flow growth, characterized by the absence of periodic change in step density on the surface, no RHEED oscillations are expected. Anyway, the absence of RHEED oscillations is not always a clear signature of pure step flow growth. Even when a steady RHEED intensity is observed, nucleation on terraces may occur. Such a mixed growth mode causes a constant step density and, therefore, a constant RHEED intensity.

It is worth to stress that a strong difference between the RHEED intensity behavior in case of 3-dimenional or step-flow growth mode is observable at

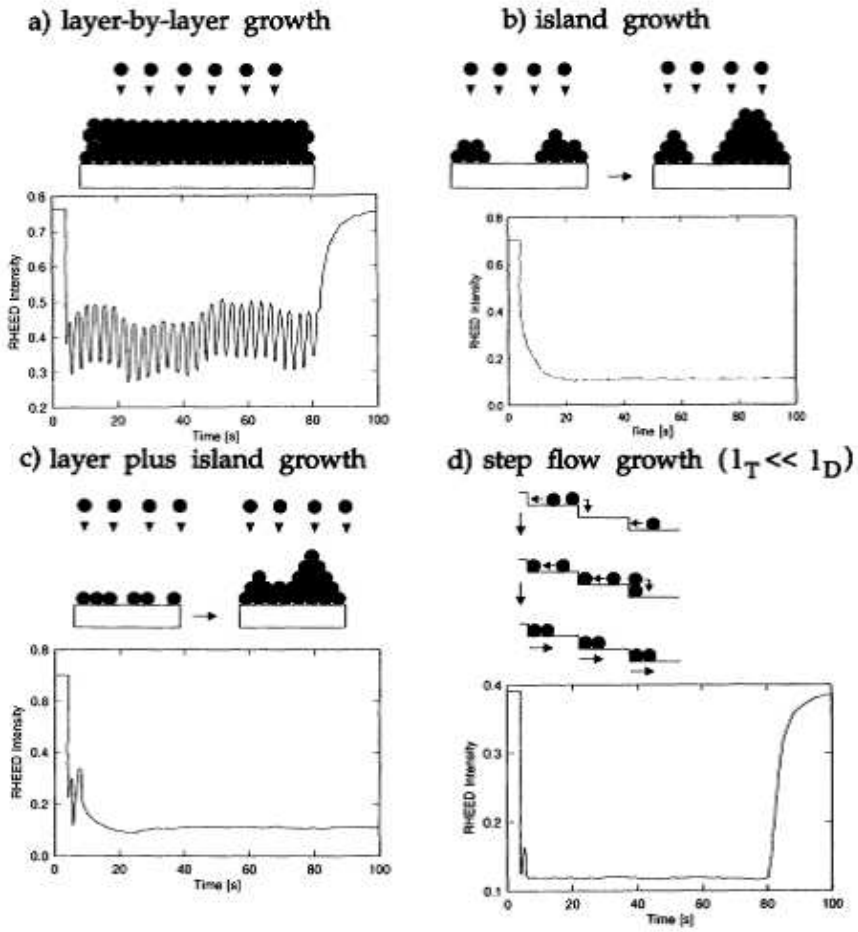

Figure 3.7: Example of (0,0) RHEED intensity variation during film deposition, for different way of growth

the end of deposition. Even if the signal strongly decrease with the first laser shots and then remains constant during the growth in both cases, in layer-by-layer growth it increase again when the deposition is stopped. In case of 3-D growth this *recovery* of the RHEED intensity takes no place.

This feature is attributable to the order degree of the surface in the two case: while in step-flow the step density remains constant during the growth, in the case of 3D growth it increases. At the end of film deposition, one get an ordered two-dimensional surface in the first case, and a extremely disordered surface in the second case.

3.7 Phase shifting in RHEED oscillations

Since it was first reported in the early 1980, the observation of the intensity oscillation of a *specularly* reflected spot, is routinely used in measuring the deposition rate and determining the film growth mode.

Instead, intensity oscillations of non specular beams have been not systematically studied, even though they have the same period of the specular one and, sometimes, show greater variations in intensity then the specular beam. However, the non specular spots oscillations exhibit an interesting phenomenon of phase shift with respect to the specular spot.

Although this phenomenon is well known and widely discussed in literature, its origin is still unclear. Fundamentally, the main interpretations are two: some authors address the phenomenon to the geometrical conditions of diffraction, others found its origin in the electrons multiple scattering, that usually are neglected in the kinematic approximation and the phenomenological step-density model, the earliest and still commonly applied to interpret RHEED results.

To support the first hypothesis, some authors performed a phase shift study between (0,0) and (0, $\pm$1), with respect to the diffraction conditions [85]. The interesting result was that the phase shift results to be very sensitive to the incident grazing angle of the e-beam on the surface. In particular, one group [86], found out that a phase shift exists even between the the oscillations of the same (0,0) spot, recorded after changing the diffraction conditions.

From the point of view of the second group, the origin of phase shift is not geometrical but physical, being due to inelastically scattered electrons. In this frame, some groups suggest that interaction with Kikuchi lines may be responsible for the change of phase, when a RHEED intensity measure is performed on spots too near that features. For this second groups, the phase shift information deepens the analysis of surface dynamics using RHEED. For example, recently, Braun et al.[87] studied the additional phase of reflection high energy electron diffraction (RHEED) intensity oscillations at heterointerfaces. They claim that the evolution of the phase shift for the (0,0) and (0,1) streaks of the same RHEED pattern is different because the two streaks show a different sensitivity on surface morphology: whereas diffraction into (0,1) streaks requires good lateral periodicity of the surface, no lateral periodicity is required for diffraction into the (0,0) streak. Therefore, they conclude that the signal on the (0,0) streak should be most sensitive towards steps running along the electron beam, while the (0,1) beams sample mostly terraces. The phase shift phenomenon has led to the use of dynamical diffraction theory accounting for multiple scattering. Such calculations

are, in some cases, qualitatively consistent with the measurements [88], but significant discrepancies continue to be unexplained [89].

During the present work, we noticed such feature, recording simultaneously the intensity variations of the specular spot (0,0), together with (0,±1) spots. An example of the acquired experimental data is showed in Figure 3.7: as can be seen, the three all spots exhibit an oscillatory behavior, with the same period of oscillation but with a phase shift of about 180°. Is to say that the value of the phase shift we found in our measurements was not always the same. Anyway, we do not try to explore if this aspect was related to geometrical diffraction condition or to inelastic scattering of the electrons on the surface. In fact, in the contest of the present work the attention was focalized on RHEED features much closer related to thee aspects of the growth kinetic.

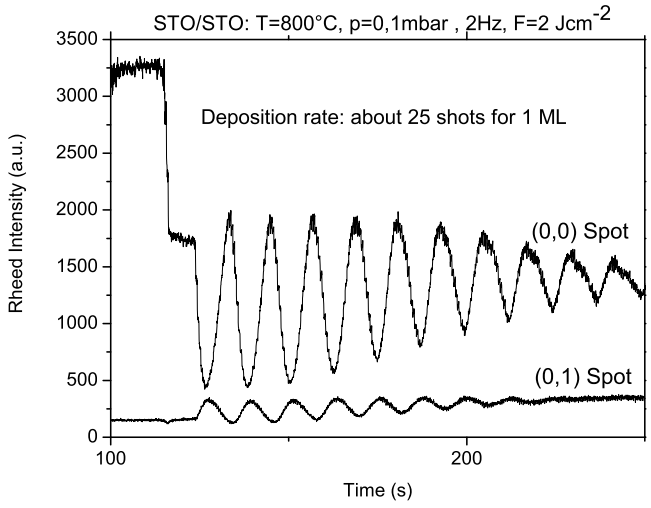

Figure 3.8: Phase shift between (0,0) and (0,1) spots RHEED intensity oscillations. The (0,-1) spot signal was overlapped to (0,1) one and was not shown.

Chapter 4

Fast photography results

Fast ICCD photography in situ diagnostic was proved as a very suitable technique for monitoring plume expansion during thin film deposition [57], [58], [59], especially due to the advantage of providing spatially resolved two-dimensional intensity maps of the three-dimensional plume expansion. Although this technique only monitors species which are optically active in the visible range, it was shown [90] that it provides a description of the plume expansion which is consistent with different complementary techniques, such as optical emission spectroscopy and ion probe, which only provide a local probe. Fast side-on images of the plume propagation in the ambient gas were obtained by recording the overall visible self-emission of the plasma plume. This allowed obtaining information on the effects of the ambient gas during the different stages of the plume expansion. The analysis was carried out at different oxygen background gas pressures in the typical range used for $La_{0.7}Sr_{0.3}MnO_3$ and $SrTiO_3$ thin film deposition, and for a deposition temperature T_s ranging from room temperature, RT, up to T=900 °C.

Besides evidencing a significant difference in the kinetic energy of plume particles, according to the oxygen background pressure, our data clearly demonstrate a considerable reduction of the background gas resistance to plume propagation as the substrate temperature was increased. The observed phenomena lead us to conclude that the deposition temperature influences film growth not only through its direct thermal effect on surface kinetics of adatoms, but also by affecting the energetic properties of the precursors in the gas phase.

We interpret the results in a simplified model of plume front propagation, accounting for the change in the background gas density induced by the substrate temperature.

4.1 Ambient gas effect on plume propagation

Nanosecond laser irradiation produces a plasma plume whose light emission is visible soon after the laser pulse strikes the target surface. The evolution of the plume at later times can be studied by recording this emission as a function of the time delay after the laser pulse hits the target.
It should be noticed that the images acquired by fast photography show the spectrally integrated emission from the excited states of the various species in the plasma plume. They may not be representative of the total flux of particles, since part of the plume is nonluminous. Nevertheless, as mentioned in the previous introduction, the analysis of the plume images has been largely employed as a diagnostic technique of laser ablation plume [91],[92],[93],[94] and is capable of revealing different interesting effects occurring during the propagation of the ablated species in the background gas, which will be discussed below.
As the ambient gas pressure increases, the plume expansion dynamics is determined by the interaction of the plasma species with the background gas molecules, which results in a change in the properties of the plasma emission. In order to describe the plasma plume propagation in the ambient gas, $La_{0.7}Sr_{0.3}MnO_3$ plume snapshots at p=0.05 mbar, p=0.1 mbar and p=0.2 mbar, with substrate-heater held at room temperature, are shown in Figure 4.1.

The most important issues of the plume-gas interaction process, clearly visible in the plume snapshots displayed in Figure 4.1, are:

- the influence of the ambient gas on the luminous plume shape and structure,
- the broadening of the plume and the effect of the background gas pressure, and
- the stopping of the plume at high pressure.

At background gas pressure p=5×10^{-2} mbar, the plume is characterized by a more forward peaked expansion, with respect to the case of higher pressure values. Furthermore, we observed a change in the internal structure of the plume, with the formation of a double-peak distribution of the maximum intensity emission (red color, in our scale).

The peak maximum, initially visible at the plume tail, progressively moves towards the plume edge as a consequence of the deceleration of the plume front and the confining effect of the background gas. In particular, a second peak appears at the front of the plume as a consequence of the interaction

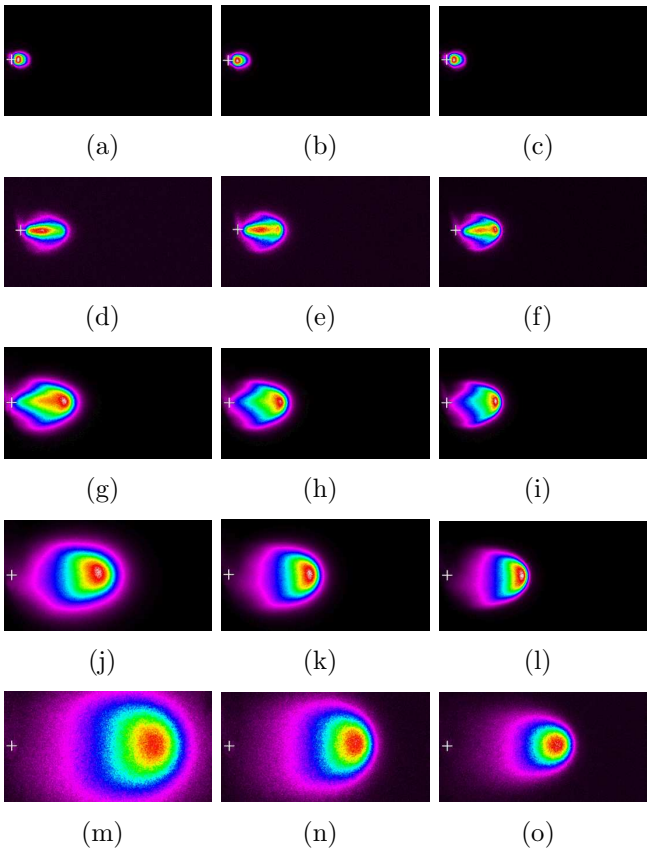

Figure 4.1: $La_{0.7}Sr_{0.3}MnO_3$ plume image at RT, t=200 ns (a)(b)(c), t=580 ns (d)(e)(f), t=950 ns (g)(h)(i), t=2100 ns (j)(k)(l), t=6600 ns (m)(n)(o), for p=0.05 mbar (left), p=0.1 mbar (center), p=0.2 mbar (right). The white cross indicates the position where the laser hits the target.

with the background gas molecules. The relative intensity of this second peak increases with time, and finally, the two peaks merge forming a single structure close to the plume front. At larger times most of the emission comes progressively from the region close to the plume front as a consequence of the formation of a contact surface to the background gas and the related *snowplough* effect, i.e. the confinement of the ablated species in a thin layer in the contact region with the environmental gas. For a time delay of $t\sim$ 600 ns, this phenomenon is well visible for an oxygen pressure of p= 0.2 mbar and it's just hinted for p= 0.1 mbar, while for p= 0.05 mbar, the maximum of emission distribution is still situated in the plume edge near the target.
It is interesting to note that, when this spatial plume splitting occurs, the plume front still follows an almost free propagation. Only successively the plume front starts to brake (as can be clearly seen in the following Figure

4.2).

This means that the plume splitting results from the transmission inside the plume of the initial interaction between the ablated species at the plume front and the background gas molecules. This occurs during the formation of a plume-background gas contact front.

The spatial splitting is likely to be due to plume species which are scattered in a backward direction during collisions with background gas molecules and interact with the incoming particles, forming a secondary density maximum closer to the plume front. Subsequently, a significant adjoint mass of background gas is present at the plume periphery leading to the formation of a contact front and to a progressive braking of the plume expansion. This, in turn, produces the accumulation of a large part of the ablated species at the plume front, leading to the plume sharpening observed at longer times and larger pressure.
Moreover, the collisions experienced by the ablated atoms with background gas molecules, beyond losing their kinetic energy, also affects the angular distribution of the plume species, which is an important aspect of the propagation process. At early times the angular distribution is peaked strongly in the forward direction, independently from the environment pressure. Then, a significant broadening is observed by increasing the time delay. In general, looking at the third column in Figure 4.1, relative to an oxygen pressure of p=0.2 mbar, one can observe that the higher is the pressure value, the broader is the plume.

We used the plume images acquired during the plasma expansion to obtain position-time plots of the leading edge of the plume self-emission along the normal to the target surface, shown in Figure 4.2. In the inset the plume front velocity, measured as the derivative of the position-time plot is shown as function of the distance from the target surface.

Plume front dynamics in the early stage of expansion (time $\leq$1 μs and position $\leq$1 cm) is almost linear irrespective of the gas pressure, and the ejection velocity is about 12 Km/s. At later times, when the plume front position is around 2 cm, the braking effect due the oxygen pressure, is well appreciable. At a deposition pressure of p=0.05 mbar, the plume reaches the substrate [1] after 10 μs. Instead, at p=0.2 mbar, even after 20 μs the plume front has not yet reached it. Furthermore, as the pressure is raised, the plume impacts the substrate at a progressively reduced velocity, coming almost at rest near the substrate for a pressure of p=0.2 mbar at RT.

[1] target-substrate distance of 4.0 cm

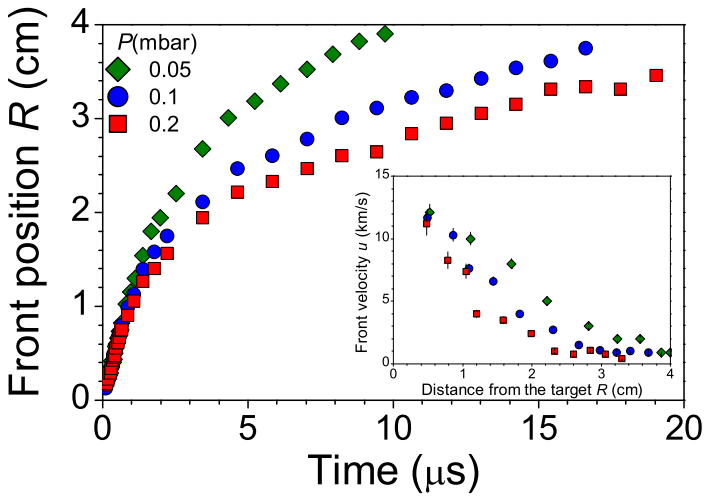

Figure 4.2: Distance-time plots of the plume front at three different oxygen background gas pressures. Inset: plume front velocity u as a function of the distance along the normal to the target surface R.

4.2 Substrate temperature effect on plume propagation

As mentioned in the introduction of this chapter, we performed a second set of measurements, in which we fixed the deposition pressure, and observed the plume expansion behavior for different values of the substrate-heater temperature. The main interesting result shown by these measurements is that the resistance of the background gas to plume propagation is strongly modified by the heating of the whole environment, that takes places during high temperature deposition.

Once fixed the deposition pressure at p=0.2 mbar, we recorded the self-emission of the expanding plume for several values of the substrate–heater temperature. In Figure **??**, the ICCD images of $La_{0.7}Sr_{0.3}MnO_3$ plasma plume for three value of substrate temperature are reported: T=300°C, T=600°C and T=900°C. It is worth to notice that pretty similar results

were also observed in the case of laser ablation of $SrTiO_3$.

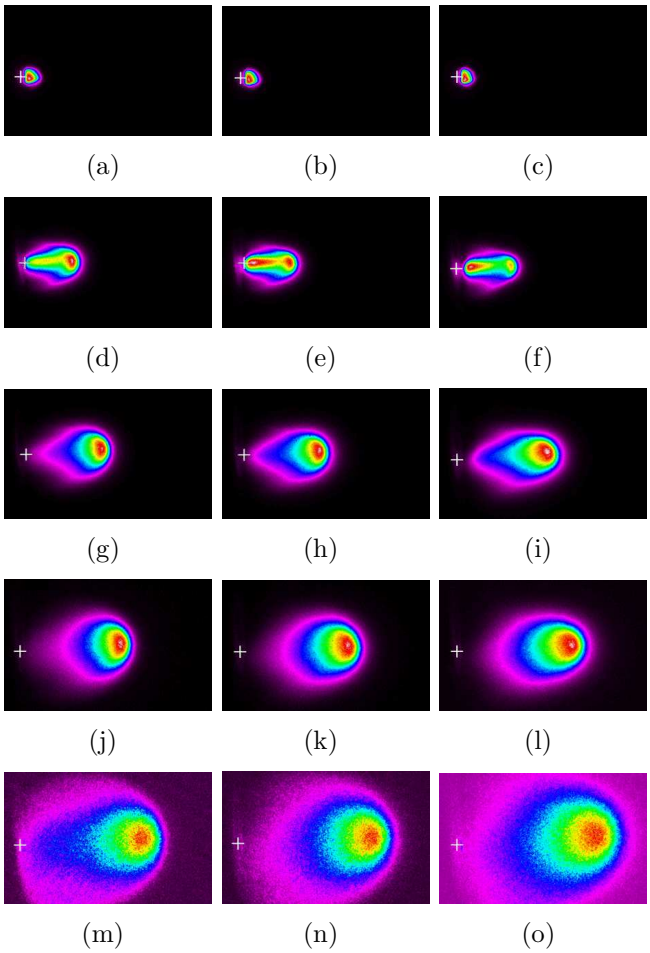

Figure 4.3: $La_{0.7}Sr_{0.3}MnO_3$ plume image at p=0.2 mbar, t=200 ns (a)(b)(c), t=950 ns (d)(e)(f), t=2100 ns (g)(h)(i), t=3600 ns (j)(k)(l), t=6600 ns (m)(n)(o), for T=300 °C (left), T=600 °C (center), T=900 °C (right). The white cross marks the position where the laser hits the target.

The comparison of the three columns clearly indicates that the resistance of the background gas to plume propagation is strongly modified by the heating of the whole environment that takes places during high temperature deposition.

In the early stage of the plume expansion, no differences are visible in the plume shape and length. Indeed, after 950 ns from the laser shot, a modification in the internal structure of the plume with respect to the substrate temperature is clearly visible, even if at this stage the plume length is not

yet significatively affected. In fact, looking at the expansion along the direction of expansion, one can see that the maximum intensity (red color, in our scale) is near the edge of the plume, in proximity of the target or in both position, according as the substrate temperature is T=300 °C, T=600 °C or T=600 °C, respectively. That is, a clear plume front as a consequence of the interaction with the background gas molecules is already formed at 950 ns only for the lower temperature. Moreover, also the angular broadening change with the substrate temperature: for a fixed delay t the plume become more "tapered" (more forward peaked expansion) increasing the temperature from 300 °C to 900 °C.

From 2100 ns ahead, the maximum in intensity remains localized at the edge of the plume, in the contact region with the ambient oxygen. In addition, increasing the time delay after the laser shot, the plume dimension along the normal to the target surface is progressively longer at T_h=900 °C than at RT (room temperature), indicating a reduction of the resistance offered by the ambient gas as the substrate-heater temperature increases. All the previous plume features, observed with respect to different deposition temperature, are interpreted as a consequences of a modification of the oxygen density profile along the direction normal to the target, triggered by the substrate heating. In a qualitative way, one can imagine that the substrate heating process influences the ambient gas inducing a density gradient from the target to the substrate. The higher is the substrate temperature, the lower is the oxygen density encountered by the expanding plume en route to the substrate.
In this sense, the confining effect of the background gas is expected to be weaker at higher deposition temperature. The plume snapshots showed in the previous Figure **??** seems to confirm the hypothesized trend: the snow-plough effect and the slowing down of the plume, caused by the collision with the oxygen molecules, take place earlier at lower temperature, that is when the gas density is higher.

The main idea at the base of this picture is developed in details in the following, by using position-time plots of the leading edge of the plume self-emission along the normal to the target surface (see Figure 4.4).

As T_h increases, the plume front propagates with reduced resistance on the way to the substrate, arriving earlier and with a larger impact velocity. However, the front dynamics still remains unaffected by the temperature increase for the first microsecond, thus indicating that the substrate-heater temperature induces changes to the ambient gas which starts influencing the plume propagation from a distance of 1 cm from the target surface. The data of Figure 4.4 clearly indicate a faster plume front at higher substrate-heater

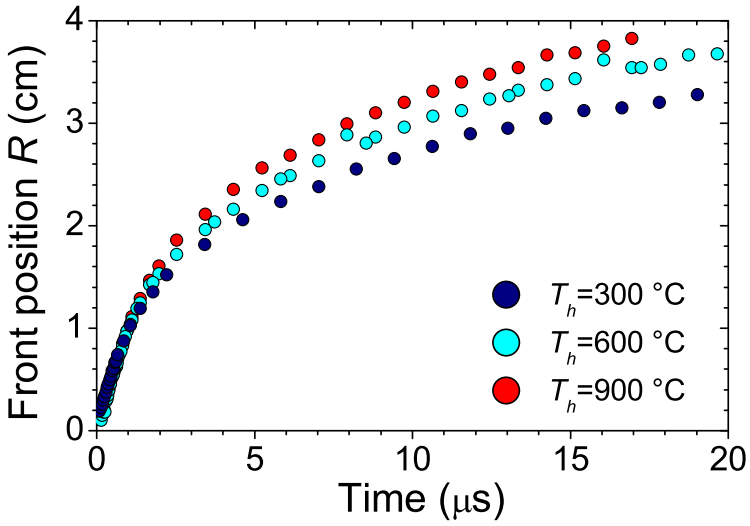

Figure 4.4: R-t position-time plots of the plume front for three different values of the substrate-heater temperature T_h at a pressure of 0.2 mbar for $La_{0.7}Sr_{0.3}MnO_3$.

temperature.

The remarkable change in the velocity of the species impacting the substrate during film growth with respect to the substrate temperature is clearly observable in Figure 4.5. The data clearly indicate a faster plume front at higher substrate-heater temperature: the velocity increases by a factor of 2-3 by passing from RT to 800-900 °C.
Moreover, the rate of change of the velocity increases for higher temperatures. This clearly indicates that the impact velocity of the ablated species is different for different values of T_h.
Similar data were collected during the ablation of the $SrTiO_3$ target, yielding consistent results. Therefore, the substrate-heater temperature indirectly changes the kinetic energy of the precursors in the gas phase. For instance, by considering an average mass of the cations of ≈100 u in both case of $La_{0.7}Sr_{0.3}MnO_3$ e $SrTiO_3$, the impact kinetic energy E_k can increase from ≈0.03-0.05 eV at T_h=300 °C to ≈0.2-0.3 eV at T_h=800-900 °C. Then, the temperature increase causes a crossover from a regime of largely thermalized particles ($E_k \approx k_B$T) to a regime of hyperthermal particles.

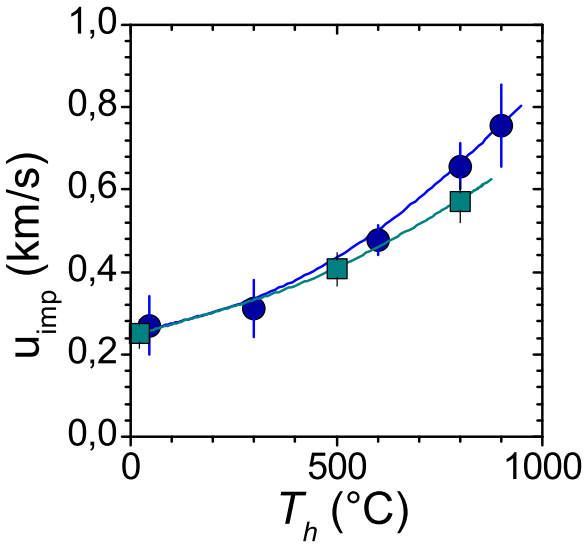

Figure 4.5: Plume front velocity at a distance of 3.5 cm from the target surface as a function of the substrate-heater temperature for $La_{0.7}Sr_{0.3}MnO_3$ (circles) and $SrTiO_3$ (squares) (the lines are guides to the eye).

The progressively reduced density encountered by the expanding plume en route to the substrate leads to a reduction of the confining effect of the background gas, and a consequent increase of the impact velocity, as the deposition temperature T_s is increased.

In the following we illustrate the model predictions, the conclusions of which are illustrated here in the case of $La_{0.7}Sr_{0.3}MnO_3$ and $SrTiO_3$, but should be applicable to other systems as well, in similar experimental conditions.

4.3 Interpretation of experimental data

We discuss our data on the plume front dynamics (see Figs. 4.2 and 4.4) by using a simple physical approach based on the balance between plume linear momentum variation and the external pressure force [56], described in details in section 3.4.
The model considers plume and adjoint background gas as a hemispherical thin layer of radius R moving at velocity u and experiencing the force due to the background gas pressure p_0 [27]. For the sake of the simplicity here the sketch model of plume-ambient gas interaction, already shown in section 3.4, is depicted again in Figure 4.3:

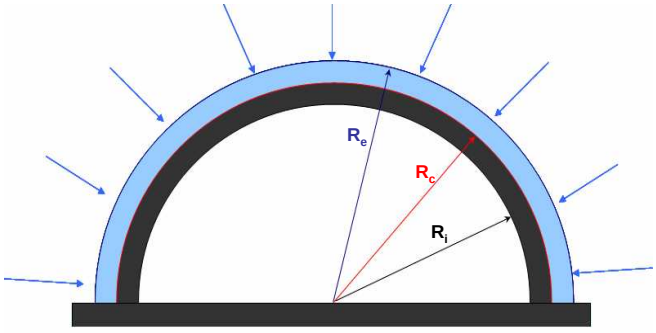

Figure 4.6: Sketch of the Predtechensky and Mayorov plume gas interaction model: the boundary of the plasma plume R_i, of the external shock wave R_e and of the contact front R are shown.

Defining with p_0 the background gas pressure and with M_p the confined plume mass, the equations of motion for R and u. u=dR/dt is the radial velocity of the layer at time t, read:

$$\frac{d}{dt}[(M_p + M_g(R))u] = -2\pi R^2 p_0 \qquad \frac{d}{dt}(R) = u(t) \tag{4.1}$$

with he initial conditions R(t=0)=0 and u(t=0)=u_0, where u_0 is the initial velocity of the plume, assumed equal to the plume front velocity in vacuum. It is worth to stress that the confined plume mass has been considered as the whole ablated mass. Actually, the really confined plume mass is a

changing quantity as the ablated species are progressively trapped by the gas layer as a consequence of collisions with the background gas atoms/molecules. However a changing mass of the confined plume will result in a more complicate model, which cannot be afforded analytically, even because it is not easy to evaluate how the confined plume mass changes with time [2].

The mass of the background gas swept away by the expanding plume at a distance R at time t is given by:

$$M_g(R) = \int_0^R \rho_g(r) 2\pi r dr, \tag{4.2}$$

where ρ(r) is the background density profile as a function of the radial coordinate r.

Considering first the results at RT (shown inFigure 4.2), when a constant density profile ρ(r)= ρ_0 can be taken into account, we have numerically solved the Eq. 4.1, thus obtaining fits to the experimental data by using an iterative minimization procedure.
From the fitting procedure estimates of the initial plume velocity u_0=(12± 1) km/s (in good agreement with the literature [73], [53], [74]), and a confined plume mass M_p=(5.3± 0.4)10^{-10} kg were obtained.
Figure 4.7 shows that the model describes pretty well the front plume dynamics and the dependence of the front velocity on the distance from the target surface.

In the aim of theoretically interpret the experimental results on deposition temperature effect on plume expansion dynamics, we extended the Predtechensky et Mayorov model. The basic idea of the model we developed here was that the substrate heating process, that takes place during the pulsed laser deposition, induces a temperature gradient between substrate-heater and target. To such temperature profile corresponds, in turn, a spatial density variation of ambient gas, between substrate and target.

In this frame, in the expression of the adjoint ambient gas mass, the gas density shows a dependance on the substrate-target distance, that is ρ_g=ρ_g(R). Such spatial density variation of background gas can be derived from the profile of temperature gradient between substrate and target.

We modeled the temperature profile by depicting the system as a background gas between two infinite parallel walls (the target and the substrate-

[2]The validity of the approximation become more and more reliable as the plume expands and the confined peak is formed (i.e. long times and high pressure).

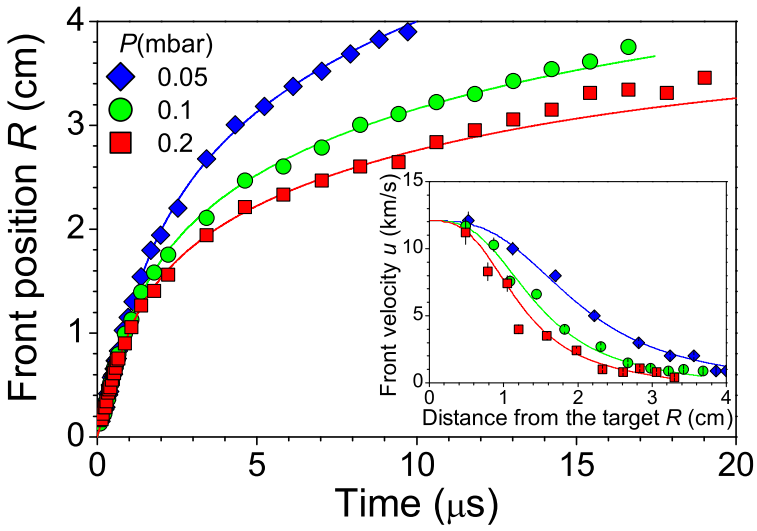

Figure 4.7: *R-t* position-time plots of the plume front for three different values of the background gas pressure for substrate heater at room temperature. Inset: plume front velocity u as a function of the distance along the normal to the target surface R. The symbols are the experimental points and the lines represent the fits according to the expansion model.

heater) held at temperatures T_{w1} and T_{w2}. In Figure 4.8 a sketch of our model is shown:

As in our experimental conditions (p= 0.1÷0.2 mbar) convection effects are negligible [95], heat transport is mainly due to conduction [96]. For the sake of simplification, we solved the heat equation by assuming an average, constant heat conductivity coefficient κ of the gas, thus obtaining a linear stationary temperature profile $T(x)$ for steady state diffusive heat transport, x being the distance along the normal to the left wall.

$$-\langle\kappa\rangle\frac{dT}{dt} = \dot{q} \tag{4.3}$$

where $\dot{q}$ is the derivative of flux.

The boundary conditions involve a temperature jump at the walls, which we assumed proportional to the normal gradient of the temperature at the boundary [97].

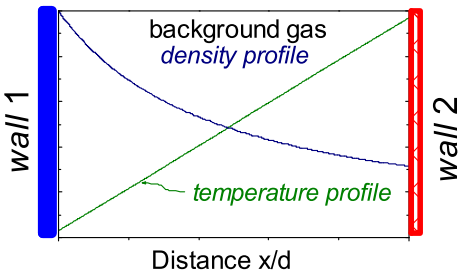

Figure 4.8: Sketch of the model system used to derive the background gas temperature and density profile along the normal to the target surface. T_L and T_R are the temperatures of the two walls representing the target (T_{W1}) and the substrate-heater (T_{W2}), respectively. Between the walls a representative temperature and density profiles obtained by solving the heat equation for steady-state diffusive heat transport used in the model

$$\triangle T = C_T \frac{dT}{dn} \tag{4.4}$$

The analytical expression for the temperature profile obtained by solving the eq. 4.3 is the following:

$$T(x) = T_L \left[1 + \frac{T_R - T_L}{T_L} \frac{x}{d}\right] = T_L (1 + \beta x) \tag{4.5}$$

where T_R and T_L are the temperatures of the two walls representing the target (*right*) and the substrate heater (*left*), respectively. As a consequence, since ρ(x)$\propto$ 1/T(x), the plume front during its motion along the normal to the target surface encounters a gas with a variable density. We assumed a gas density profile as:

$$\rho(x) \propto \frac{1}{T} \propto \rho_0 (1 + \beta r)^{-1} \tag{4.6}$$

where β is a constant which depends on the walls temperatures and boundary conditions.

After substitution of the density profile in M_g(R), we solved Eqs. 4.6 assuming β as a further fitting parameter in the minimization procedure. The results of the fitting procedure are reported as solid curves in Figure 4.9, while the corresponding density profiles are shown as inset of Figure 4.9.

The model predictions describe fairly well the behavior of the plume front dynamics observed experimentally, thus suggesting that the simple model used singles out the main basic factors related to the effects of the substrate-heater temperature on the plume expansion dynamics, in our experimental conditions. As Figure 4.9 shows, the substrate-heater temperature induces a remarkable change on the density profile of the background gas.

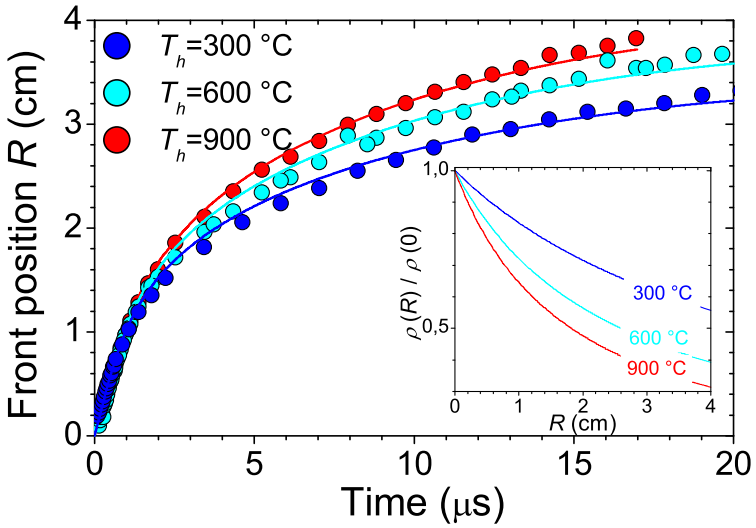

Figure 4.9: R-t position-time plots of the plume front for three different values of the substrate-heater temperature T_h at a pressure of 0.2 mbar: the symbols are the experimental points, the lines represent the model predictions. Inset: Normalized density profiles of the background gas for three different values of the substrate-heater temperature.

For example, by going from the target to the substrate the gas density decreases by a factor 1.8 at T_h=300 °C, and 3.2 at T_h=900 °C. This, in turn, results in the significant increase of the plume front velocity observed in Figure 4.5. Furthermore, the density variation also affects the plume structure, as evidenced in Figure 4.3, as a consequence of the different interplay be-

tween the plume and the adjoint mass of the background gas accumulated at the plume periphery during the expansion.

Since the variable range of the kinetic energy of the deposited particles is usually exploited to improve the thin film properties, like crystallinity and surface smoothness, such indirect effect on the kinetic energy distribution due to the deposition temperature should be taken into account in the future in selecting the most appropriate values of the deposition parameters for pulsed laser deposition.

Chapter 5

Experimental RHEED results

Reflection high-energy electron diffraction (RHEED) is a well-established and widely employed *in situ* characterization technique in thin film growth since RHEED specular beam intensity oscillations have been recognized as evidence for two-dimensional layer-by-layer growth [98]. More generally, RHEED spots intensity variation provides information regarding the growth kinetics, such as growth mode, deposition rate and diffusivity length of adatoms on the substrate surface.
In order to understand the non equilibrium film growth phenomena in a more quantitative manner, the capability of correlating the RHEED diffraction signature with the deposition parameters, such as the environmental pressure, is necessary.

The aim of the measurements presented in this chapter was to evaluate the contribution of the kinetic energy of ablated species in the film growing mechanism in PLD. Some previous studies [102], [103], [104], [108], [109] suggest that the kinetic energy of the species impinging on the substrate plays a central role in thermalization and diffusion of the adatoms, finally determining the structure of the deposit, but a totally understanding of such effect, typical of PLD process, is still missing.

The specular diffracted spot (0,0) intensity was monitored during the film deposition, changing only one deposition parameter: the oxygen pressure. That, in turn, means changing the velocity of the ablated species impinging onto the substrate, as our experimental results on plume expansion dynamics, shown in Chapter 4, section 4.3, demonstrate.
We try to correlate the modifications in RHEED oscillations plots, such as the number of oscillations, their dumping and the deposition rate, to the expansion dynamics of the plume in the corresponding experimental conditions.

While in the case of the plume expansion dynamic study, both pres-

sure and deposition temperature effects were investigated, in the film growth study presented here no RHEED measurements with respect to the substrate temperature was performed. In fact, it is well known that the migration length of adatoms on substrate surface decreases with decreasing the substrate temperature, T_s. However, we have also demonstrated that exists an inter correlations between the substrate – heater temperature deposition and the kinetic energy of the arriving atoms. The previous result implies that the change of deposition temperature would have affected not only the adatoms diffusivity, but also the kinetic energy of the species impinging the substrate. In turn, in the results of the RHEED intensity measurements performed for different substrate temperature, it wouldn't have been possible to distinguish the modification due to the difference in thermal energy from the one due to a different kinetic energy contribution of the impinging atoms.

To isolate the effect of different kinetic energy contribution, induced by changing the deposition pressure values, the study was performed only in the homoepitaxy growth case of $SrTiO_3$ on $SrTiO_3$ substrate because in the case of $La_{0.7}Sr_{0.3}MnO_3$ deposition on $SrTiO_3$, growth problems as mismatch and difference in thermal expansion coefficient could have affected the RHEED measurements, in addition to the kinetic effects we wanted to isolate.

For these reasons, in this chapter only RHEED measurements relative to $SrTiO_3$ growth for different values of deposition pressure are reported.

5.1 The problem of substrate termination

It is well known that the morphology of the initial surface, such as the substrate one, has a crucial role in the successive film growth mechanism.
In particular, it has been shown that the termination layer of the substrate does significantly influence the epitaxial growth and the stacking sequences in oxide thin films deposition [39]. In the case of heteroepitaxy of layered perovskite oxides, the termination layer of the substrate can dominantly influence the growth kinetics at the earliest stage such as wettability, mobility and sticking coefficient [99].
In the case of $SrTiO_3$ substrate, in which SrO (A-site) and TiO_2 (B-site) atomic planes are alternately stacked along the c-axis direction, most as-received substrates have mixed termination (see the pictures in Figure 5.1).

In order to obtain TiO_2 planes termination we performed an etching surface treatments of the as received substrates, i.e. a chemical procedure that implies the difference in solubility of SrO and TiO_2 in acids. To avoid the use of a too strong acid that could create etching pits also on TiO_2

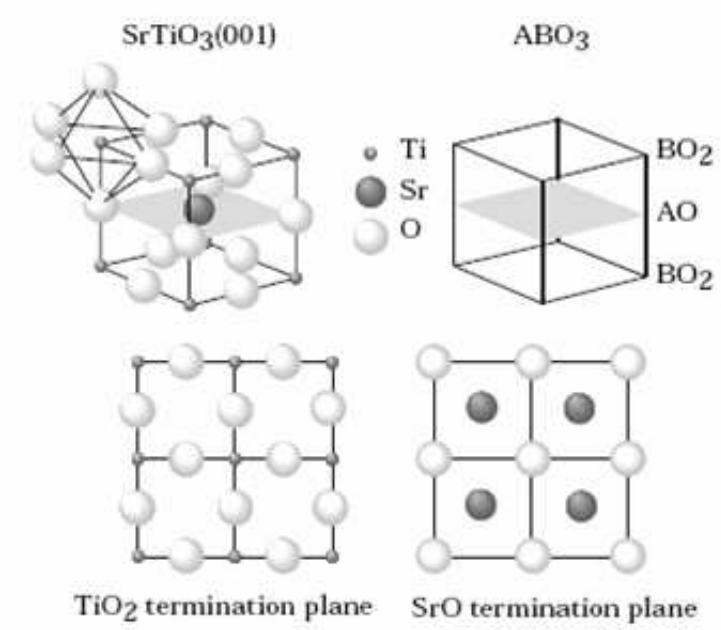

Figure 5.1: $SrTiO_3$ crystal structure and possible terminating planes of a (001) surface.

planes, the selectivity in solubility of SrO and TiO_2 was enhanced by soaking $SrTiO_3$ substrates in water [39]. SrO in the outermost atomic layer of the substrate reacts with water and forms $Sr(OH)_2$ which is easily dissolved in acidic solutions. The Sr-hydoxide complex is removed by a short dip (30 s) in a commercially available buffered HF solution (BHF). Due to this intermediate step it is possible to use a chemical solution with higher pH value, preventing etch pits to be formed. A thermal treatment inside the deposition chamber, at 950 °C and 0,5 mbar of oxygen for typically 30 min is used to obtain an $SrTiO_3$ substrate surface, ideally perfect crystalline and TiO_2 terminated. After the etching treatment on our $SrTiO_3$ substrates, we checked the obtained surfaces by STM measurements, to estimate the average values of step height and terrace length of our starting surface. In Figure 5.2 an example of such measurements made on two $SrTiO_3$ substrates, namely with (100) orientation, is reported.

The estimated terraces length of the investigated substrates ranges from l_T= 80 nm up to l_T= 400 nm. Such relevant difference in terraces length can be ascribed to the miscut between the cutting plane and the crystallographic plane of the $SrTiO_3$ crystal.

Since the aim of our measurements was estimating a possible "kinetic

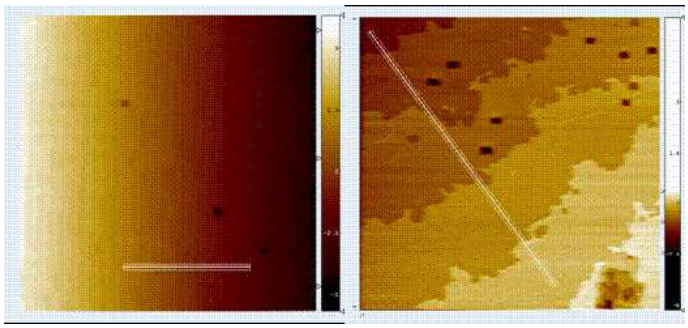

Figure 5.2: 2μm $\times$ 2μm STM pattern of two different $SrTiO_3$ substrate with a presumed (100) orientation. The estimated step length is l_T= 80 nm (right panel), l_T= 400 nm (left panel).

effect" on the film growth, it was fundamental to isolate the kinetic contribution on adatom mobility. This means avoid any other fluctuation in the experimental conditions that could have affected the RHEED measurements as much as (or even more than) the variation of kinetic energy from one deposition to the other. Such huge change in a crucial characteristic of the starting surface, as the terraces length, made it not worth to compare RHEED measurements performed on different substrates, due to the fluctuation in the step density of our substrates.

To overcome this problem we used only one substrate for all the RHEED measurements presented here, performing an intermediate *annealing* treatment between one deposition to other.

Our annealing procedure consisted in leaving the film, once deposited, on the heater in oxygen environment, increasing the heater temperature and the oxygen pressure values up to, respectively, T=950 °C and p= 0.5 mbar, for 1 hour. During the annealing time, no new material reaches the substrate surface and the growing islands travel over a longer distance forming fewer but larger islands, by coalescence, as sketched in Figure 5.3. Since during the annealing period there is no newly arrived deposit, the annealing time becomes the sole parameter in determining the final surface conditions prior to the possible subsequent deposition. A longer annealing time would result in a more complete island coalescence, that is a smaller step edge density on the surface. In this respect, it is worth to notice that some groups [100] claim that the depth of the intensity drop at the beginning of deposition can be an indication of the starting surface quality, in terms of step edges density. We noticed that the intensity variation ΔI = I_0-I_{min}, where I_0 is the intensity

before starting the deposition and I_{min} was the value corresponding to the first minimum, is the same in the three set of measurements, presented in the following. In the interpretation of these groups this should indicate initial surfaces with similar values of step density.
Our working hypothesis is that, through the annealing process, the surface could regenerate itself, becoming almost flat and smooth, independently of the deposition parameters used in the former film deposition. The validity of this experimental procedure is confirmed by other groups [101].

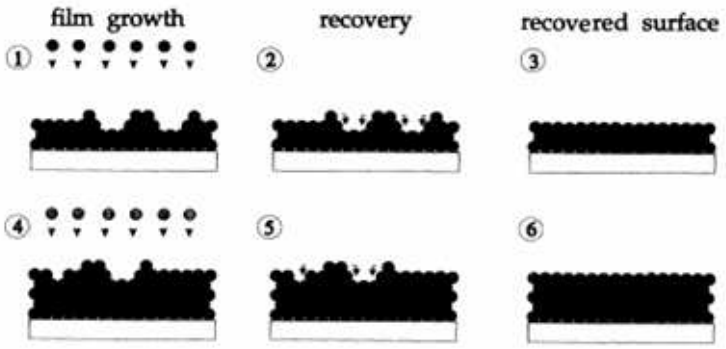

Figure 5.3: Sketch of recovery mechanism used to regenerate the surface between two consecutive depositions: after a deposition with a certain value of oxygen pressure, the annealing procedure corrects the film surface defects, enabling a sequent deposition $SrTiO_3$ on the same substrate.

The sequence of $SrTiO_3$ deposition of several tens of nm, followed by an *in situ* anneal step at T=950 °C, p=0.5 mbar oxygen pressure for 1 hour, was repeated for each film deposition performed at a fixed value of deposition pressure. The intermediate annealing step allowed to improve the surface quality obtained at the end of every single deposition. Furthermore, in some cases it enabled to regain the oscillations, even if at the end of the former deposition no more clear oscillations could be observed, because of the dumping or the appearing of the first few disordered 3D islands on the surface.

Another crucial points was the choice of the most appropriate material for the aim of studying the correlations between kinetic energy of the arriving atoms and the film growth mechanisms.

The film quality was extremely high for both $La_{0.7}Sr_{0.3}MnO_3$ and $SrTiO_3$ deposition onto $SrTiO_3$ substrate and RHEED intensity measurements showed

a regular oscillatory behavior up to several tens of nm for both compounds in the appropriate deposition conditions.

An example of the high regular growth obtained for $La_{0.7}Sr_{0.3}MnO_3$ film on $SrTiO_3$ substrate is shown in Figure 5.1, where it is reported the (0,0) RHEED intensity plot relative to $La_{0.7}Sr_{0.3}MnO_3$ deposition on $SrTiO_3$ substrate at deposition temperature T_s=650 °C, oxygen pressure p= 0.1 mbar, laser fluence F=2 J cm^{-2}, laser repetition rate ν=2 Hz.

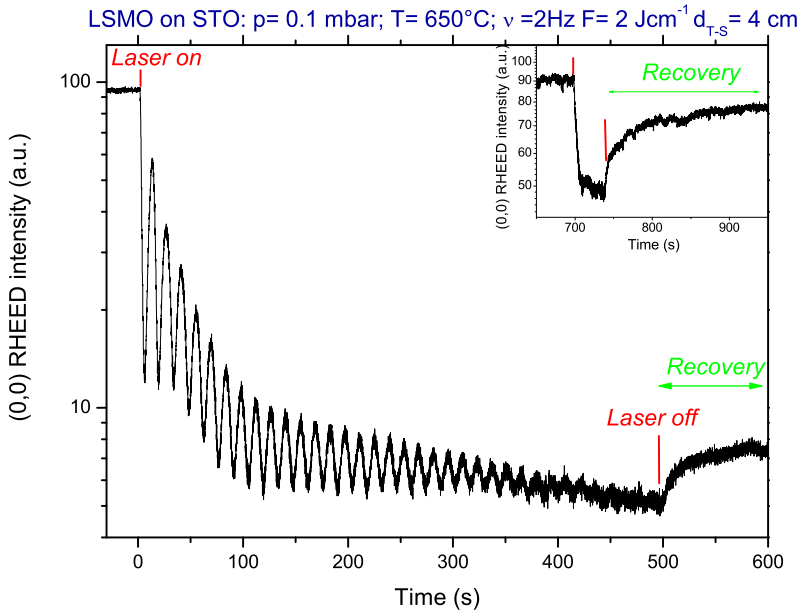

Figure 5.4: RHEED specular spot intensity measurements of $La_{0.7}Sr_{0.3}MnO_3$ on $SrTiO_3$ growth at T=650°C, **p**=0.1 mbar.

The oscillatory behavior of RHEED specular spot confirms a layer-by-layer growth mode in the selected experimental conditions: from the oscillation period a deposition rate of about 28 laser shots for 1 monolayer is estimated. The dumping in RHEED oscillations indicates a two-dimensional multilevel growth, characterized by a nucleation on an increasing number of unit-cell levels, as discussed in section 3.6.1. Nevertheless, the strong intensity recovery, at the end of deposition of about 12 nm thickness $La_{0.7}Sr_{0.3}MnO_3$ film, clearly indicates a growth surface with few defects, finally corrected by a short annealing treatments. The extremely high $La_{0.7}Sr_{0.3}MnO_3$ film surface

quality in such deposition conditions is confirmed by the RHEED pattern of the final surface of $La_{0.7}Sr_{0.3}MnO_3$ film, depicted in the right panel of Figure 5.5.

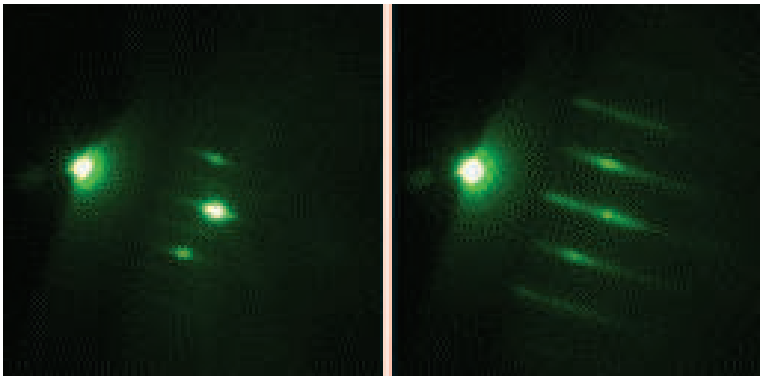

Figure 5.5: RHEED pattern of: (*left*) $SrTiO_3$ starting surface, (*right*) $La_{0.7}Sr_{0.3}MnO_3$ film deposited at T=650°C, **p=0.1 mbar**

Despite the high quality in $La_{0.7}Sr_{0.3}MnO_3$ films, we focalized our study only on $SrTiO_3$ homoepitaxy. In fact, as anticipated in the introduction of the present chapter, in case of homoepitaxy only kinetic factors determine the growth mode, whereas in case of heteroepitaxy also thermodynamic factors, e.g. misfit or differences in thermal coefficients, are also relevant. In addition, $SrTiO_3$ compound was more indicated for a kind of RHEED measurements needing an annealing procedure at high temperature, due to its chemical and compositional stability (e.g., its melting point is 2080 °C).

5.2 RHEED intensity measurements during "optimized" PLD growth of $SrTiO_3$

In this section the specular intensity measurement of an S rT iO3 homoepitaxial growth in optimized deposition conditions will be briey discussed. A RHEED measurement during the optimized pulsed laser deposition is shown in Figure 5.6, for the RHEED specular spot (0,0), and for the (0,±1) spots, which also exhibit an oscillatory behavior with the same period, but shifted with respect to the specular spot signal.

The film growth mode is layer-by-layer until the laser stops: from the oscillations period a deposition rate of 25 laser pulse for a monolayer is ob-

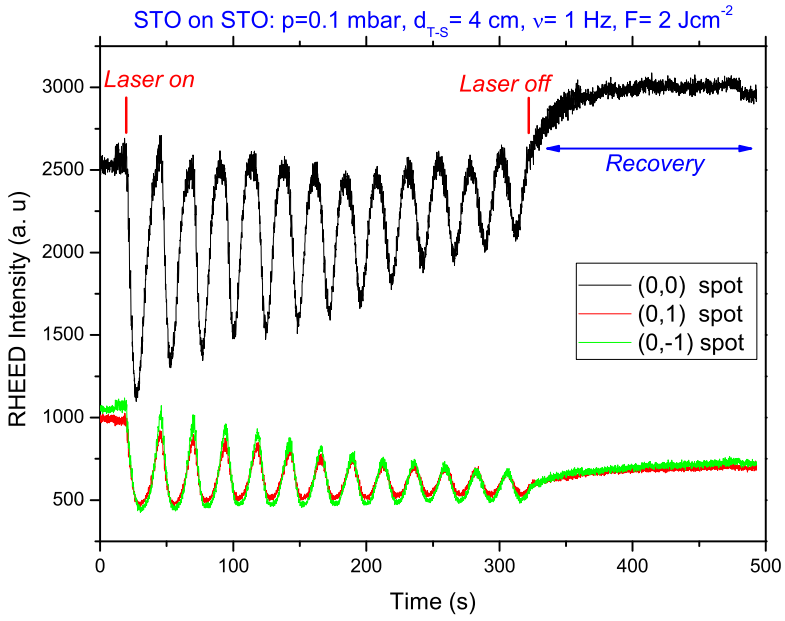

Figure 5.6: RHEED acquisition during $SrTiO_3$ layer-by layer growth, for the following selected parameters of deposition: p=0.1 mbar, T_s=800 °C, d_{T-S}=4 cm, F=2 Jcm^{-2}, ν=1 Hz.

tained, corresponding to a film thickness of 5 nm. The strong RHEED intensity recovery at the end of the deposition confirms an high quality surface with very few defects.
The Figure 5.7 shows a detail of the RHEED intensity measurements versus the deposition time where it is possible to observe the laser pulses modulation of the RHEED signal: immediately after the laser pulse, the intensity of a diffraction spot immediately drops.

This immediate drop is caused by the great increasing of the step density on sample surface, due to the the ablated material deposited onto the substrate. Between two consecutive laser pulses these clusters will diffuse toward the step edges and coalesce to form larger islands if sufficient thermal energy is present. This recrystallization process of initially disordered material results in a smoothening of the surface, a reduction of the step density and to a consequent exponential increase of the RHEED intensity, as reported by [83] and [84]. As can be seen, the characteristic relaxation time

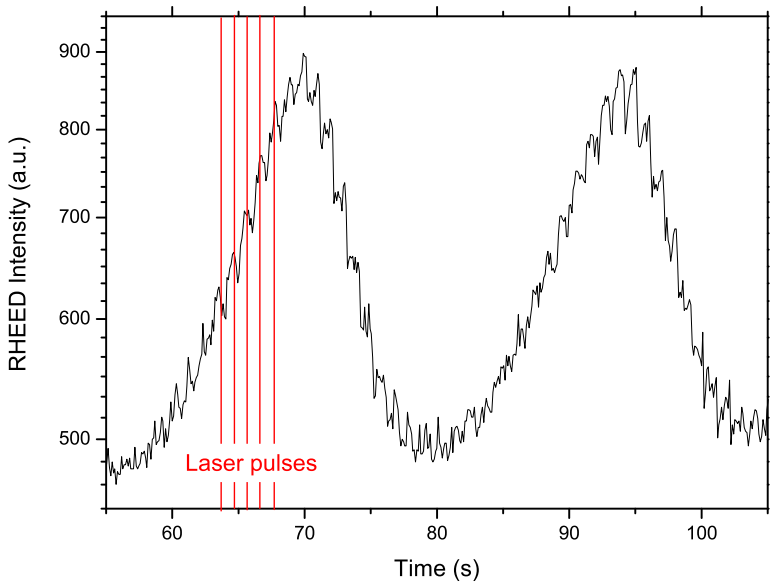

Figure 5.7: A detail of the previous RHEED acquisition: it is possible to observe the pulses laser modulation of the RHEED signal.

depends, among other things, on the coverage during deposition. This can be understood remembering that different values for the coverage mean a different step density.

5.3 RHEED intensity Oscillations vs Deposition Pressure

To check the role of the kinetic contribution to adatom mobility on the substrate surface and on film growth mode during PLD, we performed RHEED intensity measurements for three different values of the deposition pressure, that is for three different average values of kinetic energy of the impinging species. In fact, our time gated photography measurements clearly showed the role of the deposition pressure in slowing down the plume and from the plume expansion dynamics analysis we were able to estimate the values of kinetic energy with respect to deposition pressure.

Since we experimentally found that the highest film quality for $SrTiO_3$

compound is achieved at a substrate temperature around 800 °C, the study of RHEED oscillations was performed fixing the temperature to such value, so that the thermal contribution to adatom mobility was the same in all the measurements.

In the following the set of measurements, performed for three different values of deposition pressure, as to say for three different values of kinetic energy E_k of the species impinging on the substrate, are discussed.

The RHEED pattern of a hetched $SrTiO_3(100)$ substrate is shown in right panel of Figure 5.8.

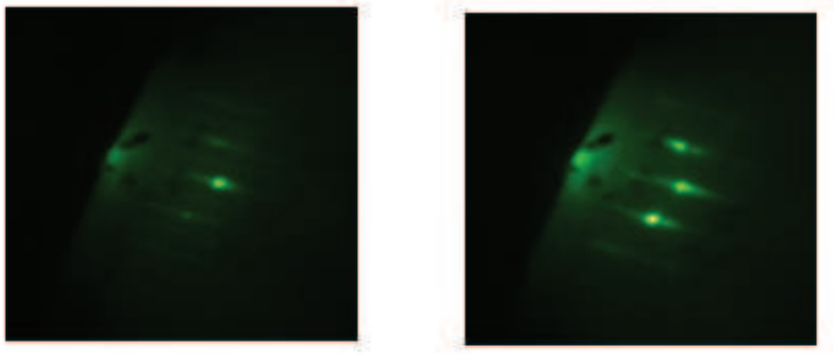

Figure 5.8: RHEED pattern of: (*left*) $SrTiO_3$ substrate, (*right*) $SrTiO_3$ film deposited at T=800°C, **p=0.1mbar**, thickness of about 11 nm

Three spots on the 0^{th} -order Laue circle, corresponding to the (0,0), (0,-1) and (0,+1) reciprocal lattice rods, are clearly visible. The occurrence in the RHEED pattern of sharp circular shape conrms the atness and the smoothness of the substrate surface. The RHEED diffraction pattern of the same surface, after a $SrTiO_3$ lm deposition of 11 nm, with a deposition pressure of p =0.1 mbar is shown in the left panel. As can be seen, the (0,1) and (0, ±1) spots became brighter and the nal diffraction pattern results in three sharp circular spots on the Laue sphere, just a little stretched out in rods. This clearly indicates a smooth nal surface, even better than the starting one. This data are conrmed by the RHEED measure of the (0,0) intensity variation during the growth, plotted in Figure 5.9.

The (0,0) spot exhibits an oscillatory behavior, typical of a *layer-by-layer* growth. The value of the maximum in intensity is going to increase during

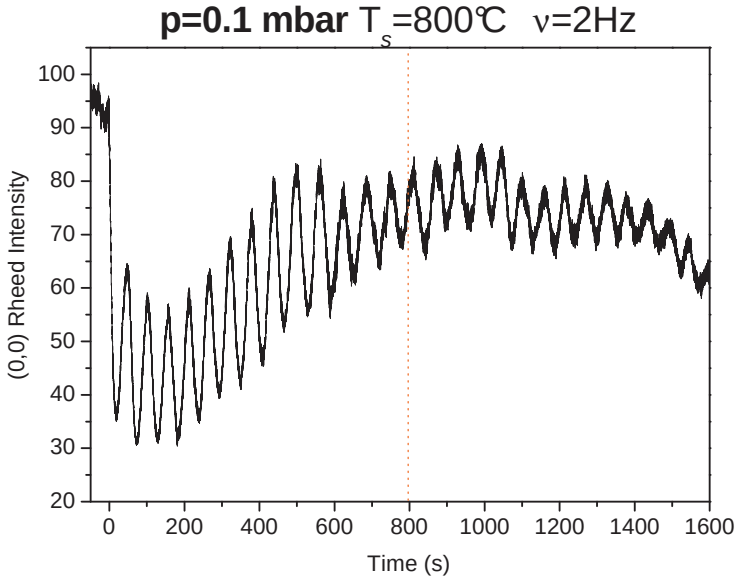

Figure 5.9: RHEED oscillations during STO deposition at T=800°C, **p=0.1mbar**

the film deposition, so indicating an enhancement of surface flatness with respect to the starting substrate. From the period of the oscillations we estimated a deposition rate of 110 shots for 1 layer. Such value, bigger than the usual one of about 25 shots for ML we got for our "standard" deposition conditions, is justified by the fact that we worked in low fluence condition. In this way, we increased our sensitivity to modification in deposition rate due to kinetic effect of the plume. From the plume dynamics analysis performed in the same experimental conditions [1] (see Chapter 4), we estimated an average value E_k for the kinetic energy of the ablated species arriving on the substrate of few tens of eV, and the plume stopping distance $d_{stop} > d_{T-S}$, the distance target-substrate.

After a long annealing, for totally recovering the surface, we checked again the RHEED pattern of the starting surface for a new $SrTiO_3$ deposition, this time with a value of p=0.2 mbar for O_2 pressure in the chamber. All the others experimental parameters were unchanged. In Figure 5.10 the starting and final RHEED patterns, after the second $SrTiO_3$ deposition are showed, while in Figure 5.11 the (0,0) spot intensity variation vs deposition time is reported.

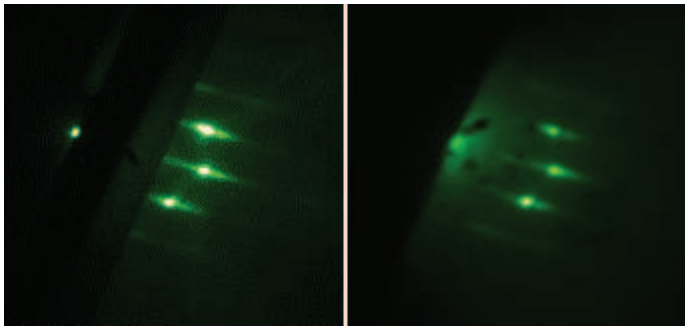

Figure 5.10: RHEED pattern of: (*left*) STO starting surface, (*right*) STO film deposited at T=800°C, **p=0.2mbar**

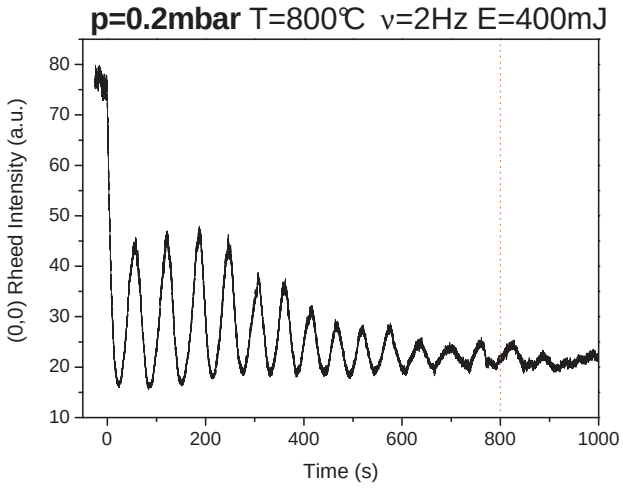

Figure 5.11: RHEED oscillations during $SrTiO_3$ deposition at T=800°C, **p=0.2mbar**

The (0,0) RHEED intensity exhibits again an oscillatory behavior, indicating again a *layer-by-layer* growth, but the oscillations start to be dumped after the first 4 ML. The resulting decreasing of the growing surface quality is confirmed by the comparison of the RHEED patterns showed in Figure 5.10. For this value of the deposition pressure in the PLD chamber, the estimated average kinetic energy E_k is of few tenth eV, while the plume stopping distance is $d_{stop} \leq d_{T-S}$, the distance target-substrate. The estimated deposition rate, in this case, is of about 120 shots for 1 ML, little higher than the value corresponding to lower pressure.

[1] d_{T-S}=4 cm, F_l=2 Jcm^{-2}, ν=2 Hz

Finally, after annealing again the obtained surface to a complete recovery, we performed an $SrTiO_3$ deposition changing again only the deposition pressure, that was set to p=0.05 mbar. With this value of oxygen pressure, the estimated kinetic energy is of several tens eV, and the plume stopping distance is bigger than the deposition distance, i.e. $d_{stop} \gg d_{T-S}$. In this case, as shown in Figura 5.12 the RHEED oscillations of (0,0) spot are strongly dumped, thus indicating that the surface is evolving from a single-level system to a multi-level system. This results from a growth mechanism in which nucleation on top of 2D islands takes place before completion of a unit-cell layer. Still, one can speak of a 2D growth mode. However, nucleation and incorporation of adatoms at step edges is proceeding on an increasing number of unit-cell levels.

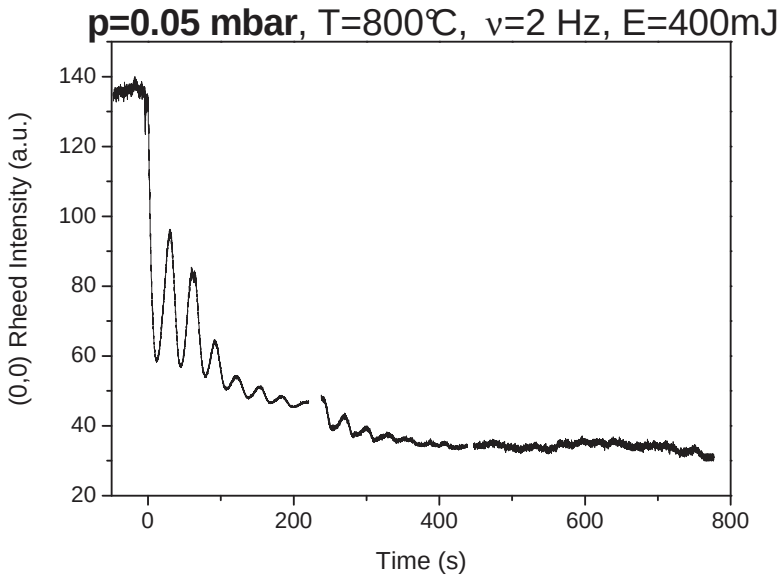

Figure 5.12: RHEED oscillations during STO deposition at T=800°C, **p=0.05mbar**

The final surface aspect is showed in Figure 5.13, panel (b). The circular spots (0,0) and (0,±1) are now strongly blurred into rods. This is an indication of a more disordered surface, even if not yet totally 3D: the additional diffuse spots, originate from the transmission of the electron beam through the small 2D islands. Furthermore, it is interesting to note that, in this case, the deposition rate was of about 60 laser shots for 1 layer, corresponding to

half of the value for a double pressure.

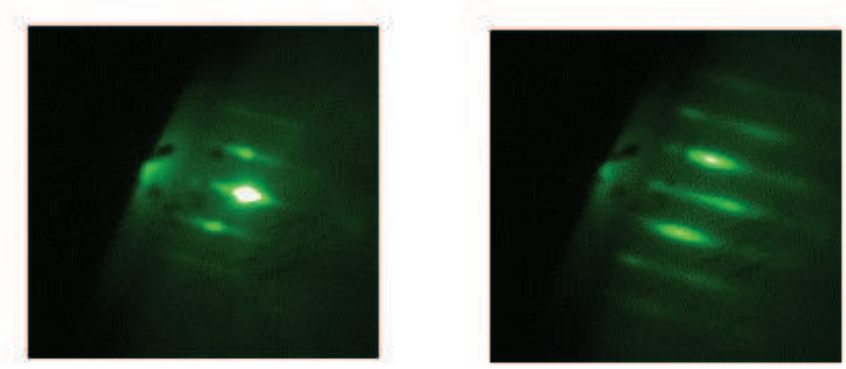

Figure 5.13: RHEED pattern of: (*left*) $SrTiO_3$ starting surface, (*right*) $SrTiO_3$ film deposited at T=800°C, **p=0.05 mbar**

In the table 5.3 our experimental data on the plume kinetics parameters, that is the kinetic energy of the impinging atoms E_k and the plume stopping distance d_{stop} (that is the average path of the ablated species before they thermalize), and on the film growing characteristics, such as the occurrence of intensity oscillations and the deposition rate are summarized. The values of the kinetic energy are shown in comparison with the estimated value for the activation energy that, in the case of a TiO_2 terminated $SrTiO_3$ substrate, is about E_A=3.8 eV [101].

p (mbar)	E_k (eV)	d_{stop}vs d_{T-S}	Dep. Rate	E_k vs E_A	Oscillations
0.05	tens of eV	$d_{stop}>d_{T-S}$	60 shots for 1 ML	$E_k > E_A$	Strongly dumped
0.1	few eV	$d_{stop}\sim d_{T-S}$	110 shots for 1 ML	$E_k \sim E_A$	YES
0.2	tenth of eV	$d_{stop}<d_{T-S}$	120 shots for 1 ML	$E_k < E_A$	Dumped

Table 5.1: For each investigated deposition pressure, the values of the kinetic energy of the species impinging onto the target (E_k), compared to the activation energy (E_A) for ($SrTiO_3$) substrate, the film deposition rate (*Dep. Rate*), the comparison between the plume stopping distance (d_{stop}) and the target-substrate distance (d_{T-S}) and the intensity oscillations occurrence are summarized

Our fast photography data evidenced the effect of the oxygen pressure value on the average kinetic energy of the atoms impinging on the substrate and on the plume stopping distance. The RHEED data have shown the role of such parameters in determining the film growth mechanism, affecting the film deposition rate and, in a more indirect way, the film growth mode. We found that the higher is the deposition pressure, the lower is the deposition rate: in particular the deposition rate double, changing the pressure value from 0.05 mbar to 0.1 mbar, while it does not change so significantly passing from 0.1 mbar to 0.2 mbar. We believe that this happens because in the pressure range around 0.2 mbar, the plume stopping distance is much shorter than the target–substrate distance. For this reason the ablated species that reaches the substrate are already thermalized and their "kinetic history" has no influence on the deposition rate.

The comparison between our experimental data on RHEED intensity oscillations for the three pressure values, p=0.05 mbar, p=0.1 mbar and p=0.2 mbar, seems to suggest that the stability of layer-by-later growth is enhanced by a "correct" contribute in kinetic energy of the plume.

Below a pressure value, all the arriving particles are expected to be thermalized, since the plume lenght becomes smaller than the target-substrate distance and the relaxation time, in this condition, is almost independent of the deposition pressure and it is mainly governed by the thermal energy term E_{th}=k_BT. Here it is worth to stress that such thermal contribution, even if it is smaller [2] than the average value of E_k of the impinging atoms, represents the main contribution in adatoms surface mobility since it acts for the whole film deposition process, a timescale much longer then the one of plume kinetic contribution (few μs).

The increasing of the kinetic energy from few tenth of eV up to some eV promotes a more stable layer-by-layer growth, corresponding to a high quality smooth surface growth, presumably because of the enhancing of the adatoms surface diffusion that reduces the effective energy barrier [105], [107], [106], [108], [4]. A further increase of the kinetic energy up to several tens of eV seems instead to deteriorate the surface of the growing film, probably creating small defects that can not be recovered by the adatoms growth kinetics.

[2] k_BT is about 0.1 eV at T_s=800 °C

Conclusions

This work dealt with the study of pulsed laser deposition of complex oxides by means of two complementary techniques, such as time gated fast photography and reflection of high energy electron diffraction. This allowed investigating two main distinct aspects of pulsed laser deposition process - i.e. the plume expansion and the film growth - thus highlighting the direct correlations among them. Such correlated study provides the opportunity of gaining a deeper understanding of the effect of the various processing parameters on the final film quality, allowing a fine tailoring of the experimental conditions in view of the desired film properties. Such quantitative approach to pulsed laser deposition is particularly relevant in the case of complex transition metal oxides, since it is known that their properties can be modified in a dramatic way by minor structural and compositional tuning. Only a careful control of thin film growth can therefore allow their application in the fabrication of electronic or spintronic devices. Among the wide class of complex transition metal oxides, the present work focused on $La_{0.7}Sr_{0.3}MnO_3$ and $SrTiO_3$ compounds. The plumes dynamic expansion was investigated, with respect to both the background gas pressure and the deposition temperature, by means of a fast ICCD based technique providing spatially resolved two dimensional intensity maps of the three dimensional expanding plume.

Beside evidencing the braking effect on plume expansion due the deposition gas, our data revealed also an indirect effect on the plume dynamic due to the deposition temperature. We observed a considerable reduction of the background gas resistance to plume propagation as the substrate-heater temperature was increased, leading to a remarkable change in the velocity of the species impacting the substrate during film growth and in their stopping distance. The experimental results were interpreted in the framework of a simple model, yielding quantitative agreement with our experimental findings. This, in turn, allowed elucidating the influence of the deposition temperature on the density profile of the background gas and on plume expansion towards the substrate.

Our results point to the presence of an interesting cross–correlation among

the deposition parameters which is usually overlooked in the usual empirical approach used by PLD growers. In particular, our findings demonstrate that the optimization of the PLD parameters, such as gas pressure and target-substrate distance, should be performed also taking into account the deposition temperature. In fact, the deposition temperature affects film growth not only through its direct thermal effect on surface kinetics of adatoms, but also by affecting the energetic properties of the precursors in the gas phase. The analysis of the experimental results also allowed us to estimate the average kinetic energy and the stopping distance for both $La_{0.7}Sr_{0.3}MnO_3$ and $SrTiO_3$ compounds in the typical range used for PLD of complex oxides, showing that the higher is the deposition pressure, the lower is the kinetic energy of the arriving particles.

For the investigation of the role of the kinetic energy of the impinging species on film growth mechanisms, we performed RHEED intensity measurements during the deposition, in the case of $SrTiO_3$ homoepitaxy. In fact, in case of homoepitaxy the growth mode is determined only by kinetic factors, meanwhile in case of heteroepitaxial growth (e.g. $La_{0.7}Sr_{0.3}MnO_3$ on $SrTiO_3$) other factors like misfit or differences in thermal coefficients play a relevant role. In addition, the $SrTiO_3$ compound was the most suitable for this kind of analysis due to its chemical and compositional stability which allow reconstructing a high quality surface through high temperature annealing in oxygen ambient.

In order to isolate the kinetic contribution of the ablated species on film growth mode we fixed the deposition temperature, thus ensuring an identical thermal contribution E_{th} to the adatoms mobility, and varied the value of the deposition pressure from one deposition to the other. So doing we actually varied the average kinetic energy E_k of the species impinging onto the substrate as well as the plume stopping distance d_{stop}. The RHEED data were, then, interpreted in terms of variation of the plume propagation features obtained from the fast photography acquisitions in the same experimental conditions. The results of our analysis suggests that the kinetic energy of the impinging species, in a certain range of values, might influence the stability of the layer-by-layer growth. In particular, it indicates that the properties of the impinging species may be tuned by properly selecting the various experimental parameters, and when the different role played by each one is well-clarified one can open up the route to a higher control of the deposition process and optimization of the film growth.
Finally, it is worth stressing that a deeper knowledge of the various and complex aspects involved in the PLD technique, besides its overall experimental simplicity, can be addressed only by making a step forward in the experimental characterization through the employment of various complementary

techniques. This approach, which is also at the root of the present work, is going to be progressively considered in different PLD research laboratories aiming to exploit the full potential of the technique in film growth of complex materials.

Ringraziamenti

Sono molte le persone che desidero ringraziare per aver contribuito, con ruoli diversi ma ugualmente importanti, al lavoro di ricerca di questi tre anni di dottorato. Il primo e più importante grazie va al Dott. Salvatore Amoruso e al Dott. Fabio Miletto Granozio, supervisori della presente tesi. È complicato esprimere, senza risultare formali, la riconoscenza al loro costante impegno nell'accompagnarmi e spesso guidarmi nei meandri della ricerca scientifica. Quel che vorrei riuscire a trasmettere qui, tuttavia, è un ringraziamento che va al di là dell'ufficialità del rito, perchè assieme agli insegnamenti scientifici sono stati prodighi di tempo, attenzione e pazienza. Ancora, e con l'aggravante dei ringraziamenti "arretrati" per la tesi di laurea, voglio ringraziare il Dott. X.Wang per la sua versatilità scientifica e per la sua infinita disponibilità. È poi doveroso ringraziare il Dott. Milan Radovic' per la collaborazione alle mie ricerche e per gli interventi a cuore aperto sul sistema MODA, in tutte le sue parti, senza cui molte misure non sarebbero state possibili, il Prof. Umberto Scotti di Uccio e il Prof. Riccardo Bruzzese per le proficue discussioni sui risultati delle misure ed, ancora, i componenti del gruppo di ricerca MODA, in tutte le sue diramazioni e sottogruppi. Un contributo decisivo ma (non me ne vogliano gli amici fisici) non esattamente di tipo scientifico è stato dato dalla presenza dei tanti amici che mi hanno accompagnato in questi anni, supportandomi e sopportandomi. Non credo sia necessario fare l'elenco dei nomi, spero che ognuno di loro si riconoscerà in questi ringraziamenti, che rendo stringati solo per contenere la mia smodata tendenza al sentimentalismo. Un grazie speciale va a Raffaele, che occuperà sempre un posto importante nel mio cuore. Infine, ma solo in ordine di apparizione in questo spazio, un ringraziamento enorme va alla mia famiglia, che ogni giorno mi fa sentire fortunata, coccolata ed amata.

Bibliography

[1] S. E. Park and T. R. Shrout, *J. Appl. Phys.* 82, 1804 (1997).

[2] B.Shin, *Study of Thin Film Growth Kinetics of Homoepitaxy by Molecular Beam Epitaxy and Pulsed Laser Deposition* PhD Thesis Harvard University(2007)

[3] J. M. Warrender, M. J. Aziz *Phys.Rev.B* 75, 085433 (2007)

[4] E.Vasco, C.Zaldo *J.Phys.: Condens.Matter*16, 8201 (2004)

[5] S.G.Mayr, M.Moske, K.Samwer, M.E.Taylor, H.A.Atwater *Appl.Phys.Lett.* 75 4091 (1999)

[6] J. Z. Sun et al. *R. Soc. Lond. Ser.* A 356, 1693 (1998).

[7] K. S. Takahashi, A. Sawa, Y. Ishii, H. Akoh, M. Kawasaki, and Y. Tokura, *Phys. Rev. B* 67 (2003)

[8] C.N.R. Rao, B. Raveau *Colossal Magnetoresistance, Charge-ordering and Related Aspects of Manganese Oxides*, Eds. World Scientific (1998)

[9] E. Dagotto, *Nanoscale Phase Separation and Colossal Magnetoresistance*, Springer-Verlag, Berlin (2002)

[10] I.H. Inoue, *Semicond. Sci. Technol.* 20, S112 (2005)

[11] H. A. Jahn, E. Teller, *Proc. Royal Soc. London* 161, 220 (1937)

[12] A.M. Haghiri, J. P. Renard *J.Phys.D: Appl.Phys.* 36, 127 (2003)

[13] J.E.Han, E.Koch, O.Gunnarsson *Phys.Rev.Lett.*84, 6 (2000)

[14] C. Zener, *Phys Rev.* 81, 440 (1951)

[15] M. N. Baibich, J. M. Broto, A. Fert, F. Nguyen Van Dau, F. Petroff, P. Eitenne, G. Creuzet, A. Friederich, J. Chazelas *Phys.Rev. Lett.* 61 21 (1988)

[16] G. Binasch, P. Grnberg, F. Saurenbach, W. Zinn *Phys. Rev. B* 39 (7) 4828 - 4830 (1989)

[17] K. Chahara, T. Ohno, M. Kasai, and Y. Kozono, *Appl. Phys. Lett.* 63, 1990 (1993)

[18] R.Van Helmolt, B. Holzapfel, L. Schultz, K. Samwer *Phys. Rev. Lett.* 71 2331 (1993)

[19] S. Jin, T.H. Tiefel, M. McCormack, R.A. Fastnacht, R. Ramesh and L.H. Chen *Science* 264, 413 (1994)

[20] T.Saitoh, M. Nakatake, A.Kakizaki *Phys.Rev.B* 66,035112 (2002)

[21] G.Banach, R. Tyer, W.M.Temmerman, "Study of half-metallicity in LSMO", Submitted to *Elsevier Science*

[22] Yu Lu, X. W. Li, G. Q. Gong, Gang Xiao, A. Gupta, P. Lecoeur, J. Z. Sun,Y. Y. Wang and V. P. Dravid *Phys. Rev. B* 54, R8357 (1996)

[23] M.Capizzi, A.Frova *Phys.Rev.Lett* 25, n 18, 1298 (1970)

[24] M. Kanai, T. Kawai, and S. Kawai, *Jpn. J. Appl. Phys.*, Part 2 31, L331 (1992)

[25] M.Y. Chern, A.Gupta, B.W. Hussey, *Appl. Phys. Lett.* 60, 3045 (1992)

[26] T. Terashima, Y. Bando, K. Iijima, K. Yamamoto, K. Hirata, K. Hayashi, K.Kamigaki, and H. Terauchi, *Phys. Rev. Lett.* 65, 2684 (1990)

[27] A.Sambri, S. Amoruso, X. Wang, M. Radovic, F. Miletto Granozio, R. Bruzzese, *Appl.Phys.Lett.* 91, 151501 (2007)

[28] K. van Benthema, C. Elsa, R. H. French *J.Appl.Phys.* 90, 12 (2001)

[29] R. Moos and K. H. Hardtl, *J. Appl. Phys.* 80, 393 (1996)

[30] A. Leitner, D. Olaya, C. T. Rogers, and J. C. Price, *Phys. Rev. B* 62, 1408 (2000)

[31] H. Wang, D. Cui, S. Dai, H. Lu, Y. Zhou, Z. Chen, G. Yang, *Appl.Phys. Lett.* 90, 4664 (2001)

[32] O.N.Tufte *Phys.Rev.* 155, 796-802 (1967)

[33] J.F.Schooley, *Phys.Rev.Lett.* 12, 474-475 (1964)

[34] A. Ohtomo, H. Y. Hwang, *Nature* 427, 423 (2004)

[35] E. Bellingeri, L. Pellegrino, D. Marr, I. Pallecchi, A. S. Siri *J.Appl.Phys.* 94, 9 (2003)

[36] K.A. Muller, *Phys. Rev. B* 19, 3593 (1979)

[37] J. H. Haeni et al., *Nature* 430, 758 (2004)

[38] M.Itoh et al., *Phys.Rev.Lett.* 82,3540 (1999)

[39] G.Rijnders, *The initial growth of complex oxides: study and manipulation*, PhD Thesis, University of Twente, The Netherlands

[40] University of Cambridge, Dissemination of IT for the Promotion of Materials Science, www.doipoms.ac.uk

[41] J.J.Harris, B.A.Joyce, P.J.Dobson *Surf. Sci* 103 L90 (1981)

[42] C.E.C. Wood *Surf.Sci.* 108 L441 (1981)

[43] G. Rijnders, G. Koster, D. H. A. Blank, and H. Rogalla, *IEEE Trans. Appl.Supercond.* 9, 1547 (1999)

[44] G. Rijnders, G. Koster, D. H. A. Blank, and H. Rogalla, *Appl. Phys. Lett.* 70, 1888 (1997)

[45] G.Binning, C.F.Quate, Ch. Gerber *Phys.Rev.Lett.* 56, 930 (1986)

[46] H. M. Smith and A. F. Turner, *Appl. Opt. 4*, 147 (1965).

[47] Venkatesan, T.; Wu, X.D.; Inam, A. and Wachtman, J.B. *Appl. Phys. Lett.* 52, 1193 (1988)

[48] D. Dijkkamp, T. Venkatesan, X. D. Wu, S. A. Shaheen, N. Jisrawi, Y. H. Minlee, W.L. McLean, and M. Croft, *Appl. Phys. Lett.* 51, 619 (1987).

[49] A. Inam, M. S. Hegde, X. D. Wu, T. Venkatesan, P. England, P. F. Miceli, E. W.Chase, C. C. Chang, J. M. Tarascon, and J. B. Wachtman, *Appl. Phys. Lett.* 53, 908 (1988).

[50] T.Gibert, B.Dubrueil, M.F.Barthe, J.L.Debrun, *J.Appl.Phys.*, 74, 3506 (1993)

[51] A.D. Boardman, B.Cresswell, J.Anderson, *Appl.Surf.Sci.*, 96-98, 55 (1996)

[52] C.R.Phypps et al, *J.Appl.Phys.*, 64, 1083 (1988)

[53] S.I.Anisimov, B.S.Luk'yanchuk, A.Luches *Appl.Surf.Sci.*, 96-98 (1996)

[54] R.K.Singh, J.Narayan, *Phys.Rev.B*, 41, 8843 (1990)

[55] N.Arnold, J.Gruber, J.Heitz *Appl.Phys.A* 69 S 87-93 (1999)

[56] M. R. Predtechensky and A. P. Mayorov, Appl. Supercond. 1, 10-12, 2011 (1993).

[57] S.S. Harilal, C.V. Bindhu, M.S. Tillack, F. Najmabadi, A.C. Gaeris, *J.Appl. Phys.* 93 2380 (2003)

[58] S. Amoruso, A. Sambri, M.Vitiello, X. Wang, *Appl.Surf.Sci.* 252, 4712 (2006)

[59] D.B. Geohegan, *Appl. Phys. Lett.* 60 2732 (1992)

[60] T.E.Itina, A. A. Katassonov, W. Marine M. Autric *J.Appl.Phys.* 83, 11 6050 (1998)

[61] R. F. Wood, K. R. Chen, J. N. Leboeuf, A. A. Puretzky, and D. B. Geohegan *Phys. Rev. Lett.* 79, 1571 - 1574 (1997)

[62] P.B. Allen, *Phys.Rev.Lett.*, 59, 1469 (1987)

[63] P.B.Corkum et al, *Phys.Rev.Lett*, 61, 2886 (1988)

[64] D.Bauerle *Lasers Processing and Chemistry* -3^{rd} Ed. Springer, Berlin (2000)

[65] J.F.Ready, *Effects of High-Power Laser Radiation*, Academy Press, New York (1971)

[66] A.Peterlongo, A. Miotello, R.Kelly *Phys. Rev. E* 50, 4716 (1994)

[67] S.I.Anisimov,B.S.Luk'yanchuk *Physics* 45, 293-324 (2002)

[68] M.I.Kaganov, I.M.Lifshitz, L.V. Tanatarov, *Sov.Phys JEPT* 4, 173 (1957)

[69] B. N. Chichkov, C. Momma, S. Nolte, F. von Alvensleben, and A. Tnnermann, *Appl.Phys. A* 63, 109 (1996)

[70] S. Nolte, C. Momma, H. Jacobs, A. Tnnermann, B. N. Chichkov, B.Wellegehausen, and H. Welling, *J. Opt. Soc. Am. B* 14, 2716 (1997)

[71] Ya.BZel'dovic, Yu.P.Raizer, *Physics of shock waves and high temperature hydrodinamic phenomena* Academic Press, New York, (1966)

[72] R.W. Dreyfus, *Appl.Surf.Sci* 283, 177 (1993)

[73] S.Amoruso, A.Sambri, X.Wang *J.Appl. Phys.* 100, 013302 (2006)

[74] P.E.Dyer A.Issa, P.H.Key *App.Phys.Lett.* 57, (1990)

[75] S.Amoruso, B.Toffman, J.Schou *Phys. Rev. E* 69, 05643 (2004)

[76] M.Huijben, *Tuning electronic properties by atomically controlled growth*, PhD Thesis, University of Twente, The Netherlands

[77] Frank, F.C. and Van der Merwe, J.H. *Proc. Roy. Soc. London* A 198, 216 (1949)

[78] Volmer, M. and Weber, A. *Z. Phys. Chem.* 119, 277 (1926)

[79] Stranski, I.N. and Krastanov, Acad. Wiss. *Math.-Naturw.Klasse* IIb 146, 797 (1938)

[80] J. H. Neave et al., *Appl. Phys. A* 31, 1 (1983).

[81] S.Stoyanov *Surface science*, 199, 226 (1988)

[82] S.Stoyanov, M.Michailov, *Surface science*, 202, 109 (1988)

[83] H.Karl, B. Stritzker *Phys.Rev.Lett.* 69, 2939 (1992)

[84] V.S.Achutharaman, N. Chandresekhar, O.T.Valls, A.M. Goldman, *Phys.Rev.B* 50, 8122 (1994)

[85] J. Resh, K. D. Jamison, J. Strozier, A. Bensaoula, A. Ignatiev, *Phys. Rev. B* 40, 11799 (1989)

[86] B.Shin, J. P. Leonard, J. W. McCamy, M. J. Aziz *J. Vac. Sci. Technol.* A 25, 2 (2007)

[87] W. Braun, L. Daweritz, and K.H. Ploog, *J. Vac. Sci. Technol. A* 16, 2404 (1998)

[88] Z. Mitura, S. L. Dudarev, L. M. Peng, G. Gladyszewski, and M. J. Whelan, *J. Cryst. Growth* 235, 79 (2002)

[89] Z. Mitura, S. L. Dudarev, and M. J. Whelan, *Phys. Rev. B* 57, 6309 (1998)

[90] S. Amoruso, R. Bruzzese, R. Velotta, N. Spinelli, M. Vitiello, and X.Wang *Appl. Surf. Sci.* 248, 45 (2005)

[91] S. Acquaviva and M. L. De Giorgi, *J. Phys. B* 36, 247 (2003).

[92] S. Amoruso, R. Bruzzese, N. Spinelli, and R. Velotta, *J. Phys. B* 32, R131 (1999)

[93] S. S. Harilal, C. V. Bindhu, M. S. Tillack, F. Najmabadi, and A. C. Gaeris *J. Phys. D* 35, 2935 (2002)

[94] D. B. Geohegan and A. A. Puretzky, *Appl. Phys. Lett.* 67, 197 (1995)

[95] B. Bird, W. E. Stewart, and E. N. Lightfoot, Transport Phenomena (Wiley, New York, 1960)

[96] D. B. Geohegan, A. A. Puretzky, and D. J. Rader, *Appl. Phys. Lett.* 74 (1999)

[97] L. S. Pan, T. Y. Ng, D. Xu, G. R. Liu, and K. Y. Lam, J. Micromech. Microeng. 12, 41 (2002)

[98] D. Blank, G. Rijnders, G. Koster, H. Rogalla *Applied Surface Science* 127, 633 (1998)

[99] J. Choi, C. B. Eom, G. Rijnders, H. Rogalla, and D. H. A. Blank *Appl.Phys.Lett.* 79, 10 (2001)

[100] J. Y. Lee, T. C. Wang, S. F. Chen, J. Y. Juang, J. Y. Lin, K. H. Wu, T. M. Uen, Y. S. Gou *Chin. Journ. Phys* 39, 4 (2001)

[101] M.Lipmaa, N. Nakagawa, M. Kawasaki *Appl.Phys.Lett.* 76, 2439 (2000)

[102] E.Irissou, B.Le Drogoff, M.Chaker, D.Guay *Appl.Phys.Lett.* 80, 10 (2002)

[103] R. Dolbec, E. Irissou, M. Chaker, D. Guay, F. Rosei, M. A. El Khakani *Phys. Rev. B* 70, 201406(R) (2004)

[104] P.R. Willmott and J. R. Huber, *Rev. Mod. Phys.* 72, 315 (2000)

[105] M.E. Taylor and H.A. Atwater, *Appl. Surf. Sci.* 127-129, 159 (1998)

[106] H. Brune, G. S. Bales, J. Jacobsen, C. Boragno, and K. Kern, Phys. Rev. B 60, 5991 (1999)

[107] H.Jenniches, M. Klaua, H.Hoche, J. Kirchner *Appl.Phys.Lett.* 69, 3339 (1996)

[108] P.R.Willmott, R.Herger, C.M. Schleputz, D.Martoccia, B.D. Patterson *Phys.Rev.Lett.* 96, 176102 (2006)

[109] D.M. Zhang, L. Guan, Z.H. Li, G.J. Pan, H.Z. Sun, X.Y. Tan, L. Li *Surface and Coatings Technology* 200, 12 4027-403 (2006)